

Wind structure and luminosity variations in the WR/LBV HD 5980²

Leonid Georgiev¹

Instituto de Astronomía, Universidad Nacional Autónoma de México, Apdo. Postal 70-264, México D.F., 04510, georgiev@astro.unam.mx

Gloria Koenigsberger

Instituto de Ciencias Físicas, Universidad Nacional Autónoma de México, Apdo. Postal 48-3, Cuernavaca, Mor. 62210, gloria@astro.unam.mx

D. John Hillier

Department of Astronomy, 3941 O'Hara Street, University of Pittsburg, Pittsburg, PA 15260, USA

Nidia Morrell

Las Campanas Observatory, The Carnegie Observatories, Colina El Pino s/n, Casillas 601, La Serena, Chile

Rodolfo Barbá

Departamento de Física, Universidad de la Serena, Benavente 980, La Serena, Chile; ICATE-CONICET, San Juan Argentina

and

Roberto Gamen

Facultad de Ciencias Astronómicas y Geofísicas, Universidad Nacional de La Plata, and Instituto de Astrofísica de La Plata (CCT La Plata-CONICET), Paseo del Bosque S/N, B1900FWA, La Plata, Argentina

¹Visiting Astronomer, Department of Astronomy, 3941 O'Hara Street, University of Pittsburg, Pittsburg, PA 15260, USA

²Based on data obtained with HST, IUE, FUSE and the 6.5-m Magellan telescopes at Las Campanas Observatory in Chile

²Based on data obtained with HST, IUE, FUSE and the 6.5-m Magellan telescopes at Las Campanas Observatory in Chile

1. Introduction

Eruptive mass-loss phenomena in massive stars is emerging as an area of interest for many reasons, one of the most important of which is that the characteristics of certain supernova explosions depend critically on the progenitor’s mass. The stars classified as Luminous Blue Variables (LBV’s) appear to have the ability to remove a large fraction of their outer stellar layers through violent ejection processes long before the SN phase is reached. It is believed that these ejections, combined with the effects of the stationary stellar winds, may determine to a large extent the mass of the supernova progenitor (van Marle et al., 2007, Smith, 2008, Dwarkadas, 2011).

The LBV eruptions have been observed since the 1600’s, but the mechanisms driving the instability have not been identified. Although some scenarios have been suggested (Guzik, 2005, Owocki & van Marle, 2008, Kashi & Soker, 2010), their confirmation is difficult due to the large distances at which most of these objects lie and the fact that they are intensely observed only after they have undergone an eruptive event. Thus, their pre-eruption characteristics are poorly constrained. Furthermore, observational constraints on their fundamental parameters are often lacking.

HD 5980 is a multiple system in the Small Magellanic Cloud that has been observed spectroscopically since the 1960s. It contains an eclipsing binary system plus a third object. Four well-defined variability timescales are present: 1) a long-term (~ 40 years) variation (Koenigsberger et al. 2010); 2) sudden eruptive events which were observed in 1993 and 1994, each lasting less than 1 year (Barbá et al. 1995; Koenigsberger et al. 1995, Jones & Sterken, 1997); 3) orbital-phase locked variations with the 19.3-day eclipsing binary period (Breysacher, Moffat & Niemela 1982; Foellmi et al. 2008, and references therein); and 4) “microvariability” on ~ 30 minute timescale that was observed shortly after the 1993/1994 eruptions (Sterken & Breysacher, 1997). These timescales disclose the presence of a variety of physical phenomena in the system. In particular, Koenigsberger et al. (2010) have argued that the 1993-1994 eruptions may have been caused by tidal interactions that became stronger due to a gradual increase in the stellar radius, on the ~ 40 year timescale. Although the process responsible for the ~ 40 year timescale is unknown, it is believed to be the same as that which occurs in S Doradus -type variables.

The three luminous objects comprising the HD 5980 system are: two emission-line stars in a close 19.3-day binary orbit (Breysacher & Perrier 1980) and a third O-type object (hereafter *star C*) whose photospheric absorptions remain relatively stationary on the orbital timescale of the binary (Niemela 1988; Koenigsberger et al. 2002). Following the convention introduced by Barbá et al. (1996), we label as *Star A* the star “in front” at orbital phase $\phi = 0.00$ and *Star B* the one “in front” at the opposite eclipse, which occurs at $\phi = 0.36$.

Star A is the unstable star of the system (Barbá et al. 1996), and whose spectral type has changed from the Wolf-Rayet subtype WN3 (in 1978-1981; Niemela 1988) to WN6 (in 1990; Koenigsberger et al. 1994) culminating in WN11/B1.5Ia⁺ during the 1994 eruptive phase (Drissen et al., 2001; Heydari-Melayari et al., 1997; Koenigsberger et al., 1998a). *Star B* is believed to be a WN4 star (Breysacher, Moffat & Niemela 1982; Niemela 1988). Further background on HD 5980’s observational characteristics may be found in Barbá et al. (1996, 1997), Moffat et al. (1998), Koenigsberger (2004) and Foellmi et al. (2008).

Although its triple nature implies having to deal with the problem of disentangling the spectra of three stars and the possible contribution from a wind-wind interaction region to arrive at the eruptor’s properties, HD 5980 provides considerable advantages for studying the underlying instability: 1) its distance and masses can be relatively well-constrained; 2) it is un-obscured by dust; 3) it has been widely studied spectroscopically at X-ray, UV and optical wavelengths; and 4) it was well observed during the stages prior to the 1993–1994 eruptions and intensely observed thereafter. In this paper we focus on determining the epoch-dependent properties of *Star A*. Section 2 is devoted to a description of the observational data; in Section 3 we empirically disentangle the wind velocities of the three stars in the system; the existence of correlations between visual magnitude, UV brightness, emission-line strength and wind speed are shown to exist in Section 4. Section 5 contains the description of the model atmosphere fits to the spectra; the results are discussed in Section 6 and the conclusions presented in Section 7.

2. Observational material

Ultraviolet spectroscopy ($\lambda\lambda 1190\text{--}2000\text{ \AA}$) of HD 5980 is available from the *International Ultraviolet Explorer (IUE)* at low and high resolutions in 1979, 1981, 1989, 1991, and 1994–1995, and at low resolution in 1978 and 1986. The properties of these spectra were analyzed by Moffat et al. (1989) and Koenigsberger et al. (1994, 1995, 1998a, 1998b), and an overview of the derived results may be found by Koenigsberger (2004). Further UV observations at high resolution were obtained using the *Hubble Space Telescope Imaging Spectrograph (STIS)* in 1999, 2000, 2002 and 2009. The properties of these spectra are described by Koenigsberger et al. (2000, 2001, 2010). Tables 1 and 2 list in the first three columns the identifying number for each spectrum, the date of acquisition and the corresponding orbital phase computed with the Sterken & Breysacher (1997) initial epoch and orbital period. For many of the *IUE* spectra of HD 5980 a visual magnitude m_v could be derived (Koenigsberger et al. 1994) from the Fine Error Sensor (FES) counts through the FES- m_v calibrations (Perez 1992). These are listed in column 4 of Tables 1 and 2. The FES magnitudes have a formal error of 0.07

mag.

The *IUE* spectra analyzed in this paper were retrieved from the *MAST* data base, which contains spectra that have been re-processed with the Final Calibration. We find that the difference between the flux measurements made on these spectra and on the original data products are $<5\%$ for spectra obtained prior to 1992, but this difference increases significantly thereafter, in some cases being as high as 15% .³

Velocities of spectral features were measured using consistent criteria for all data sets. Columns 5–6 of Table 1 list the velocities of selected features that will be described in the next section. We find that the uncertainty in the speeds measured for the P Cygni absorption components is generally ~ 100 km/s, which we adopt throughout this paper unless otherwise noted. The sources of uncertainty include the small signal-to-noise ratio of *IUE* spectra, the contamination by lines arising from other atomic transitions and the definition of the continuum level. In general, the new velocity measurements coincide well, within the uncertainties, with those published previously.

The continuum flux at $\lambda 1850$ Å was measured on all UV spectra and is listed in columns 9 and 7 of Tables 1 and 2, respectively. The $\lambda 1850$ Å spectral region was chosen to characterize the UV continuum level because it is relatively line-free in most of the HD 5980 spectra. The integrated flux of the N IV] 1486 Å and N III 1750 Å blend was measured and the values are listed in columns 7-8 of Table 1 and 5-6 of Table 2. Both lines are clearly associated with the active state of *Star A*. N IV] 1486 Å was first seen in 1986, being absent or very weak previously. The N III 1750 Å emission was first seen during the declining phase of the 1994 eruption.⁴ It appeared as a single emission line in low resolution spectra but was composed of N III $2s^22p-2s2p^2$ and N III $2s2p^2-2p^3$ multiplets. The flux contained in the N IV] 1486 Å and N III emission lines was measured on the low dispersion spectra by fitting one or more Gaussian functions. On high dispersion spectra, the flux was obtained through direct integration over the emission feature. The largest source of uncertainty resides in the choice of the continuum level which is frequently difficult to define due to large number of variable emission lines and, on high resolution *IUE* spectra, the low signal-to-noise ratio.

The formal uncertainties in the flux calibrations of *IUE* and *STIS* data are, respectively, $\sim 6\%$ (Colina, Bohlin & Castelli 1996) and 1% (Maíz-Apellániz & Bohlin 2005). In general, the flux levels measured in high and low resolution *IUE* spectra differ by no more than the

³As described by Nichols & Linsky (1996), there were systematic wavelength-dependent discrepancies of up to 20% of the absolute flux calibration in some of the *IUE* spectra processed with previous software.

⁴There are unfortunately no UV spectra obtained earlier during this event.

quoted uncertainty. However, in the subset of observations obtained in 1994, the high resolution data display significantly weaker flux levels than the contemporaneous low resolution spectra. This situation might be due to tracking problems during the long exposures. Also, the FES counts are not available during this time period.⁵ Hence, for the analysis described in the following sections, we measured the continuum flux only on low resolution IUE data for the 1994 epoch.

An optical spectrum was obtained on 2009 November 7, at phase 0.038 using the Magellan Echellette (MagE) on the Clay 6.5m (Magellan-II) telescope on Las Campanas. We used the 1" slit providing a spectral resolution of 1 Å. Thirteen echelle orders were extracted covering the wavelength region from 3130 Å to 9400 Å. The signal-to-noise ratio ranges from 100 to 200 for a single 150 s exposure. The usual ThAr comparison lamp was used for wavelength calibration. The data were reduced using the special set of IRAF routines available for the reduction of MIKE spectra (*mtools* package; <http://www.lco.cl/telescopes-information/magellan/instruments>). Spectra of the standards Feige 110 and NGC 7293 central star observed during the same night were used to derive a sensitivity function. The individual flux calibrated echelle orders were then normalized and merged in the final spectrum.

For the modeling discussed below, four representative spectra corresponding to different observation epochs were constructed as follows:

Spectrum 1994: The low resolution *IUE* spectra SWP 53218 and LWP 29794 were combined with the optical spectrum obtained on the same date, 1994 December 30, at CTIO and described in Koenigsberger et al. (1998b). This combined spectrum covers the wavelength region from 1190 Å to 6900 Å. The orbital phase is 0.39, and this is the only spectrum not obtained at primary eclipse ($\phi=0$) that we analyze. During this epoch, the spectrum of *Star A* was dominant and, as in Koenigsberger et al. (1998b), the contribution from *Star B* is neglected.

Spectrum 2000: The *HST/STIS* spectrum obtained on 2000 April 20 at phase 0.00. This spectrum covers the spectral range 1150 to 10800 Å.

Spectrum 2002: The *HST/STIS* observation of 2002 April 4, obtained at phase 0.99 was combined with the *FUSE* spectrum P2230101 taken on 2002 July 27 at phase 0.00. The systematic long-term variations in HD 5980 were relatively small between 2002 and 2009, justifying that we combine these two spectra obtained ~ 3 months apart.

⁵No report of FES malfunction was found in the IUE Operations Summary, although a change in the Gyro 5 drift rate is reported to have occurred in October 1994 as well as the appearance of the DMU anomaly; see <http://wise-iue.tau.ac.il/ines/docs/p05.pdf>

Spectrum 2009: The *HST/STIS* spectrum secured on 2009 September 9 at $\phi = 0.99$ was combined with the Magellan-II optical spectrum obtained on 2009 November 7 at phase 0.04. As in the previous case, the long-term variability is not expected to be significant. Of greater concern is the fact that the optical spectrum was obtained 0.05 in phase later than the UV spectrum. At $\phi=0.04$ the eclipse of *Star B*’s continuum-emitting region is partial (see light curve in Foellmi et al. 2008).

3. Disentangling the wind velocities

The terminal wind speed V_∞ is generally derived from the saturated portion of the P Cygni absorption component; i.e., where the intensity reaches zero level, generally referred to as V_{black} (Prinja et al. 1990). In the case of a binary system, the maximum extent of the saturated profile corresponds to the speed of the slower wind in the system. The faster wind also has a V_{black} , but the minimum intensity level lies at the continuum level of the star whose wind is slower. Thus, as shown in Georgiev & Koenigsberger (2004), the absorption profile presents a step-like appearance. We will refer to the second V_{black} as $V_{plateau}$. For single Wolf-Rayet stars, it is generally found that for saturated lines $V_{black} \sim 0.70 V_{edge}$ (Prinja et al. 1990; Eenens & Williams 1994), where V_{edge} is the location where the P Cygni absorption meets the continuum level. The observation that $V_{edge} > V_{black}$ is generally attributed to an unspecified type of “turbulence” or to non-monotonicity in the wind. In the case of optically thin lines, the P Cygni absorptions do not reach the zero flux level. In this case, V_{edge} provides information on the maximum wind speed attained within the particular line-forming region.

Interpreting the P Cygni absorption components in HD 5980 is difficult because 3 massive and hot stars contribute to its spectrum. Koenigsberger et al. (1998a) adopted the purely empirical approach of measuring V_{black} and V_{edge} in *IUE* spectra obtained over the years 1979–1995. They found a persistent component at $V_{black} \sim -1740$ km/s indicating the presence of a stable wind with this speed and showed that the wind speed of *Star A* had undergone changes from <500 km/s to ~ 1600 km/s during and after the 1994 eruption. However, although they suspected that *Star A*’s wind speed had been as high as ~ 3000 km/s in 1979, disentangling its contribution to the P Cygni absorptions from that of the other two stars proved very challenging.

The more recent data have now clarified the picture, partly because of its greatly improved quality and partly because it has been possible to obtain UV observations during orbital phase $\phi=0.0$, when *Star A* occults *Star B*. The size of the eclipsing disk of *Star A* is a factor of 1.5 larger than *Star B* at minimum brightness (Perrier et al. 2009) and significantly larger during its more active state. It is therefore valid to assume that at orbital

phases $\phi \sim 0.0$ *Star A* eclipses *star B*'s continuum-forming disk as well as the P Cyg absorption forming region of *star B*'s wind. Thus, the P Cygni absorptions at $\phi \sim 0.0$ provide the wind speeds of *Star A* and *Star C*, without contamination from *Star B*.

3.1. *Star C*: the “third” object

Fig. 1 is a plot of the C IV 1548/1550 Å doublet observed in the *HST/SITS* spectra of 2009 (left panel) and 2002 (right panel) at orbital phase 0.99. A clear “step” is observed in the 2009 spectrum, providing two velocity values: $V_{black} = -1760$ km/s and $V_{plateau} = -2440$ km/s.⁶ The “step” is not as pronounced in the spectrum of 2002 (Fig. 1, right), but still two velocity values may be measured: $V_{black} = -1780$ and $V_{plateau} = -2210$ km/s. $V_{black} = -1770 \pm 10$ km/s is consistent with the persistent wind velocity measured by Koenigsberger et al. (1998a) for all epochs prior to 1996. Since only two stars are visible at $\phi = 0.99$, it is now clear that this stable component is formed in *Star C*. These spectra also give us the wind speed of *Star A* in 2002 and 2009, a topic to which we shall return in Section 3.3.

3.2. *Star B*: the elusive companion

Of the three distinguishable objects in HD 5980, *Star B* is the most elusive. From the 19.3d radial velocity variations and the eclipse light curve, there is no question that *Star B* is a hot and massive object. However, given that *Star A* is such a prominent source of emission-lines, it is difficult to determine the fraction of the emission-line spectrum that may be attributed to the wind of *Star B*. On the other hand, during the eclipse when *Star B* is “in front”, the wind region of *Star A* where the fast portions of its P Cygni absorption components are formed is occulted. This eclipse occurs at $\phi = 0.36$ and can be used to estimate *Star B*'s wind speed.

In 1999, 5 *HST/STIS* spectra of HD 5980 were obtained over a single orbital cycle (Koenigsberger et al. 2000), including a spectrum at $\phi = 0.36$. The line-profile of C IV 1548-50 Å at this phase is shown in Fig. 2 (right) where we observe $V_{black} = -1720$ km/s, associated with *Star C* as discussed in the previous section. In addition, there is a short plateau that ends at $V_{plateau} = -2300 \pm 100$ km/s, followed by a very extended slope over which the line rises towards the continuum level extending to $V_{edge} = 3100$ km/s. We associate the $V_{plateau}$

⁶Note that the separation between these two V_{∞} values is ~ 700 km/s, significantly greater than the separation between the two C IV doublets (500 km/s).

with the terminal wind speed of *Star B*. The value of V_{edge} is consistent with the relation $V_{black}/V_{edge} \sim 0.76$ typically observed for WR stars (Prinja et al. 1990). It is important to note that the eclipse at $\phi=0.36$ is not total, since *Star B*’s radius is smaller than that of *Star A*. However, the wind velocity component along the line-of-sight from the unocculted portion of *Star A* is rather slow and any P Cygni absorption formed in this star lies close to the rest-frame velocity. Thus, the very large value of V_{edge} is most likely associated with “turbulence” in the wind of *Star B*.

At other orbital phases the picture is not as clear, however. Two observations at elongations were obtained as part of the same 1999 set of *HST/STIS* spectra mentioned above. The elongation phases observed are $\phi=0.15$ and $\phi=0.83$, when *Star B* is approaching the observer and receding, respectively. At $\phi=0.15$ both the -2300 km/s plateau and -3100 km/s extended absorption should be clearly visible. However, the spectrum shows only $V_{edge} \sim -2400$ km/s, as illustrated in Fig. 3. This suggests that the “turbulent” component is suppressed in the regions that are viewed expanding along-the-line of sight to the observer at $\phi=0.15$. This may be a consequence of the presence of the wind-wind interaction region, an issue that will be addressed in a forthcoming paper. For the present investigation, it suffices to keep in mind that *Star B*’s wind velocity is $V_B \sim 2300$ km/s and that its contribution to the system’s spectrum is important only when it is “in front” of *Star A*.

3.3. *Star A: the eruptor*

In Fig. 2 (left) we illustrate the spectrum obtained in 1999 at $\phi = 0.05$. This phase is close to primary eclipse, and *Star A* is between us and *Star B*. Here there is no plateau in the absorption line-profile indicating that *Star A*’s terminal wind velocity is similar to that of *Star C* and both stars contribute to $V_{black} = -1720$ km/s. In Section 3.1 we determined the wind speed of *Star A* in 2002 and 2009 to be 2210 and 2440 km/s, respectively. This trend for increasing wind speeds between 1999 and 2009 is one that can be traced back to late 1994, at which time speeds < 500 km/s were recorded (Koenigsberger et al. 1998a). This is the inverse of HD 5980’s behavior in the epochs preceding the eruption; between 1979 and 1991 wind speeds steadily declined.

In the 1979 *IUE* spectrum obtained at $\phi = 0.91$ a plateau extending to $V_{plateau} = -2670$ km/s is clearly present in the C IV 1550 P Cygni absorption, followed by a gradual rise reaching the continuum level at -3200 km/s. The other spectra obtained in 1979 also display the plateau which, for example, in the case of the $\phi = 0.48$ spectrum extends to -2750 km/s. This is similar to the $\phi=0.36$ spectrum discussed in Section 3.2. But because none of the 1979-1980 spectra were obtained during eclipse, it is not possible *a priori* to

determine which of the two stars is responsible for the different fast components. However, since the speed determined from spectra obtained in other epochs when *Star B* eclipses *Star A* are ~ -2300 km/s, we are led to conclude that the ~ -2700 km/s component in 1979 corresponds to the wind of *Star A*. A similar analysis leads to the conclusion that by 1991 *Star A*’s wind velocity decreased to ~ -2200 km/s.

The individual contribution from *Star A* and *Star B* may also be identified in other P Cygni lines such as He II 1640 and N V 1240, lines to which the contribution from *Star C* is negligible. The N V line displays a flat portion, analogous to V_{black} , but which does not reach the zero intensity level. Its extent provides the velocity of the slower wind, either that of *Star A* or *Star B*, depending on the epoch. A second plateau provides the velocity of the faster wind. The measurements of these two plateaus are listed in column 6 of Table 1.

The He II 1640 line arises from a transition between two excited states, and thus, the strength of its P Cygni absorption is weaker than that of the C IV and N V resonance transitions. Here, the simplest measurement to perform is that of V_{edge} . Because there is no “black” portion in the absorption, it is not clear to what extent “turbulence” contributes to the edge velocity. In addition, some of the spectra show a break in the absorption profile, similar to the plateau seen in the resonance lines, and which may be associated with the second star in the system. The measured values of V_{edge} and of the plateau (when visible) are listed in column 5 of Table 1. We find that these values are consistent with the velocity for *Star A* derived from C IV and N V. Because the contribution from *Star C* may be neglected in N V 1240 and He II 1640, we use these lines for the analysis that will be presented in the next section.

The behavior of the 3 lines is illustrated in Fig. 4 for the epochs 2002 and 2009, showing that they all display the wind velocity increase that took place between 2002 and 2009.

A summary of our estimated wind speeds for the three stars at different epochs is given in Table 3. These speeds, as those of Table 1, are corrected for the systematic velocity of the SMC (+150 km/s) but do not include a correction for orbital motion. It is important to note that, except for the 1979-1980 epochs, the He II 1640 values of V_{edge} are systematically smaller than the values derived from C IV which are listed in Table 3. It is not clear whether this is caused by the presence of additional emission lines that “fill in” the absorption near its edge⁷ or whether this is a consequence of the excitation structure in the wind.

⁷The numerous absorptions associated with *Star A*’s active state are absent in 1979-1980

4. Empirical correlations

We have previously shown (Koenigsberger et al. 2010) that the emitted flux in the UV and optical lines increased during the pre-eruption epochs and decreased after ~ 1999 . Changes in the continuum flux levels have also occurred. Here we show the existence of 2 correlations and their corollaries:

Line strength vs. wind velocity: A decrease in the wind velocity is accompanied by an increase in the strength of the emission lines; i.e., $F_{lines} \sim V_{wind}^{-1}$. Fig. 5 shows the flux contained in the NIV] 1468 emission line plotted against the P Cygni absorption-line velocity of He II 1640 Å and N V 1240 Å. Only data from spectra obtained around $\phi = 0.00$ are plotted, so the velocity clearly corresponds to that of *Star A*.

Continuum intensity vs. wind velocity: A decrease in the wind velocity is accompanied by an increase in the strength of the continuum in the UV ($\lambda 1850$ Å) and in the visual range; i.e., $F_{contin} \sim V_{wind}^{-1}$. This is illustrated in Fig. 6, where the UV continuum flux is plotted against the wind velocity measured from V_{edge} of He II 1640 Å.

These two correlations indicate that changes in the wind velocity are accompanied by changes in the continuum forming region as well as in the more extended line-forming regions. That is, the entire wind structure is affected. It is also important to note that the UV and the visual continuum levels increase or decrease together, as illustrated in Fig. 7. Hence, the phenomenon is not simply due to a redistribution in wavelength of the continuum energy.

A corollary of the above relations is that the continuum brightness and emission line strengths increase or decrease together; $F_{cont} \sim F_{lines}$. This is illustrated in Fig. 8, where the strengths of N IV] 1486 and N III 1750 are plotted against the flux in the continuum at 1850 Å. The different epochs of observation lie in different locations within this diagram. These results suggest that the physical phenomenon causing the changes in *Star A* involves an overall increase or decrease in the energy that is emitted; i.e., bolometric luminosity variations.

Let us momentarily assume that *Star A*'s continuum emits as a black body. The ratio $F_{vis}/F_{1850} = 10^{-0.4*m(FES)}/F_{1850}$ at constant luminosity is an almost linear function of the flux at 1850 Å with F_{vis}/F_{1850} decreasing with the increasing temperature (continuous line on Fig. 9). The observed points in Fig. 9 are clearly separated in two groups. The points before the eruption and after 1995 lie along a curve similar to the one described by the black body, while the points obtained during the eruption are displaced from this correlation. The temperature decreased during the eruption but contrary to what might be expected, the absolute flux at 1850 Å increased, as seen in the observed F_{vis}/F_{1850} correlation. To account for this, the luminosity must have increased by a factor of ~ 6 (dashed line on Fig. 9). This

leads to the conclusion that the 1994 eruption involved a luminosity increase, a conclusion that is strengthened by the results of the CMFGEN modeling described in the next sections. The dispersion of the points around the black body curve during the other epochs points to some further changes in the luminosity although at a much smaller scale.

The interpretation of the line strength *vs.* wind velocity correlation is not straightforward. The larger V_∞ increases the transformed radius,

$$R_t = R_{star} \left(\frac{V_\infty/2500 \text{ km/s}}{\dot{M}/10^{-4} M_\odot/\text{yr}} \right)^{\frac{2}{3}} \quad (1)$$

(Schmutz et al. 1989) reducing the line strength. Thus, having in mind that V_∞ has been changing, one cannot directly interpret the weaker lines as a result of a lower mass loss rate. To proceed further in the interpretation of the line intensity variations it is necessary to model the spectra of *Star A*, which will be done in the next section.

5. CMFGEN models of *Star A* and *Star C*

As previously described, *Star A* undergoes two modes of large-scale variability: 1) A long term (~ 40 years) S Dor type variability and 2) An eruptive mode, as occurred in 1993-1994, shortly before the maximum of the S Dor cycle. The observed changes in lines and continuum fluxes that were described in Section 4 point to two separate physical states of the wind corresponding to these two modes. In order to gain further insight into the processes which drive the variability, we modeled the spectra obtained in 1994, 2000, 2002 and 2009 which are described in Section 2. These spectra correspond to times when the emission from *Star A* dominates over *Star B*'s emission. However, *Star C* is always present in the observations, so a model for this star was also constructed in order to adequately compare the models with the data. All comparisons are made against the sum of the fluxes from the *Star A* and *Star C* models.

We modeled the spectrum of *Star A* using a new version of CMFGEN code. In this version the spectrum forming region of the star is modeled as a hydrostatic photosphere and a wind attached to it. The wind is described with the usual β law. The photosphere is specified with its gravity ($\log g$) and temperature T_{10} at the Rosseland optical depth $\tau_{Ross} = 10$. This large value of τ_{Ross} is chosen so that models with different mass loss rates are comparable. The density of the photosphere is calculated to satisfy the equation

$$\nabla P = -\rho(g_{grav} - g_{rad}) \quad (2)$$

where g_{grav} is the specified gravitational acceleration and g_{rad} is the calculated acceleration due to the radiation pressure. The solution defines the density as a function of the radius. This defined density and the adopted \dot{M} together with the equation of continuity defines the velocity as function of the radius. The velocity increases with decreasing density and it is connected to the wind velocity at a prescribed point which we choose to be 10 km/s. Once the velocity and density structures are specified, the radiation transport equation is solved consistently with the equations of statistical equilibrium and the energy balance as described in Hillier and Miller (1998). Several iterations of this procedure are performed until the density structure is consistent with the radiation force and the temperature distribution. The reference point at $\tau_{Ross} = 10$ is usually situated at $V(r) \sim 5$ km/s, below the connection point so the model parameters T_{10} and $\log g$ apply to the underlying photosphere rather than the wind itself.

The model of the star is specified by several parameters which can be combined into two groups. In the first group, there is the chemical composition, the atomic data and the stellar mass. For the analysis of HD 5980, the values of these parameters are fixed for all epochs. The second group includes the stellar luminosity, the gravity acceleration, the temperature, the terminal velocity and the mass loss rate. For *Star C*, only one model fit was performed and we assume that all its derived parameters remain constant over time. For *Star A*, model fits were performed for each of the four spectra described in Section 2.

5.1. *Star C* model

Numerous photospheric absorption lines belonging to *Star C* (Koenigsberger et al, 2002) are clearly present in the 2009 spectrum. They were used to construct a model for this star. Hunter et al (2007) found that Si and Mg composition in B-stars in NGC 346 is ~ 0.2 of the solar abundance (Table 6). Assuming this is representative for all metals heavier than O, we adopted that chemical composition. The temperature of the model was fixed by the O IV 1339-43 Å and O III 5592 Å lines. The model parameters were adjusted to attain a reasonable fit to the depth of the He I and H I optical absorption lines, clearly visible on top of the emission lines. The wind velocity was set to the observed value of $V_{black} = 1770$ km/s and the mass loss rate was restricted to the minimal value for which the C IV 1548-50 doublet is saturated. The luminosity of *Star C* was fixed so that its continuum coincide with the “step” of the observed C IV 1548/50 doublet. We adopt the CNO abundances of Sk 80 (Crowther et al. 2002), with which the lines of O III 5592 Å, C III 1175 Å and C III 2297 Å

and N III 1183-85 Å (Fig. 10) are adequately reproduced. The adopted parameters are shown in Column 6 of Table 6 and the spectrum is shown in Fig. 11. The model derived for *Star C* does not have significant emission lines in the UV-optical region other than C IV 1548-50 Å, N IV 1718 Å and N V 1239-43 Å. The comparison between the observed absorption lines and the computed spectrum suggests a rotational velocity $V_{rot} \sin i = 80 \pm 15$ km/s and a radial velocity $V_r \sim 60$ km/s with respect to the *star A* + *star B* center of mass.

It is important to note that Schweickhardt (2000) found periodic radial velocity variations in the photospheric absorption associated with *Star C*, with $P_{starC} \sim 96.5$ days, and suggested that it is itself a binary system. Foellmi et al. (2008) also found RV variations in the OIII 5592.4 line consistent with Schweickhardt’s (2000) conclusion. It is thus important to keep in mind that our model for *Star C* corresponds to the combined spectra of two objects. A second point to keep in mind is that it remains to be determined whether this binary is gravitationally bound to the *Star A* + *Star B* pair or whether it is merely a line-of-sight projection.

5.2. Star A

In this section we describe the procedure for computing the model spectrum for *Star A*. Because *Star C* is in view at all times, the computed spectrum of *Star C* described above was added to all models of *Star A* before comparison with the observed spectrum. In the cases when only the normalized observed spectrum is available we compared the observations with a model flux calculated as

$$F(model) = \frac{(F_{\lambda}(starA) + F_{\lambda}(starC))}{(F_{cont}(starA) + F_{cont}(starC))} \quad (3)$$

5.2.1. Chemical composition

We constructed a fairly complex model including most of the important atoms in several ionization stages (Table 4). The main properties of the wind were obtained for each epoch. If the observed spectrum at one epoch required an adjustment of the chemical composition, the change was made in all four epochs and the models were recalculated and the consistency checked.

The He composition was determined by the decrement of the H I and H I+He II optical lines. We fitted the lines in the spectrum obtained in 1994 and found that $N(He)/N(H) =$

1.0 ± 0.2 by number. This value was fixed for all 4 spectra. Due to the significant abundance of He, the mean atomic mass of the gas is larger than the Solar. In order to be able compare *Star A* with other objects having different He/H ratios we present the composition of all other elements by their mass fractions.

The carbon abundance was constrained mainly by C IV 5804/12 Å and C III 1178 Å as observed in the 2002 FUSE spectrum. The strong C IV 1548-50 doublet is not sensitive to the abundance. The N IV 7123 Å line was used as a nitrogen abundance indicator, and consistency was checked using the UV N III, N IV and N V lines. Several iterations on all models at all epochs were made until a consistent abundance of nitrogen was obtained.

We do not observe any strong oxygen lines in the spectrum. The O IV 1338-41 Å observed in *STIS* spectra are formed in *Star C*'s wind. The weakness of these lines in *Star A*'s spectrum sets an upper limit to the O composition to 0.1 of the SMC value (1/50 of the solar composition). The phosphorus abundance was set to 0.05 solar. The predicted P V 1118-28 Å lines based on this value agree with the 2002 observations. S V 1502 Å line was fit with a sulfur abundance equal to 0.05 solar. The same abundance fits reasonably well S VI 933 Å as well. Aluminum abundance of 0.1 solar fits Al III 1855/63 Å doublet observed in the 1994 spectrum.

Finally, we adopted $\text{Fe}/\text{H} = 0.1 (\text{Fe}/\text{H})_{\odot}$ by mass since this abundance reproduces well the Fe V and Fe IV lines in the spectra of the 2000, 2002 and 2009 epochs. This iron abundance is lower than the one adopted for star C ($\text{Fe}/\text{H} = 0.2 (\text{Fe}/\text{H})_{\odot}$) but we did not perform a rigorous analysis of the abundances of *star C* and we cannot exclude that it has the same Fe/H abundance $\sim 0.1(\text{Fe}/\text{H})_{\odot}$ as of *star A*. Nevertheless we kept the Fe/H abundance of *star C* to the commonly accepted value. The lower iron abundance of *star A* is consistent with the result derived from a comparison of the wind-eclipse effects in HD 5980 and the Galactic WR system HD 90657 (Koenigsberger et al. 1987).⁸ For the elements Ne, Ar, Cl, Ca, Cr, Mg and Ni, we adopted a 0.1 times Solar composition similar to the iron abundance. The spectrum does not show any observable spectral features arising from these species but they are important for the line blanketing and the radiation force and were included in the model.

The composition of all other elements included in the model was also set to 0.10 of the solar value. The final chemical composition adopted for the four epochs is shown in Table 5. Note that the overall abundance for *Star A* is 0.1 Solar while that which was used for the *Star C* model is 0.2 Solar. The uncertainties in the model fits lead to uncertainties in the

⁸This result refers to the Fe abundance in *Star B*'s wind, derived from a comparison between the Fe V pseudocontinuum and the N IV 1718 Å line.

chemical compositions of ± 0.1 dex, so that these two metallicity values are consistent, within the uncertainties.

5.2.2. *Wind velocity*

The calculated spectrum of a model is sensitive to several parameters. The first two parameters are the wind velocity law and the terminal speed, V_∞ . The Fe V and Fe VI lines in the $\lambda\lambda 1270\text{--}1450$ Å region are optically thinner than the stronger lines present in the spectrum, and thus they are more sensitive to properties of the inner wind regions, particularly the velocity law. We find that a $\beta \geq 2$ velocity law adequately reproduces their line-profiles. Values of $\beta < 2$ produce profiles with a more “box-like” shape than observed. Thus, we set $\beta = 2$. The value of V_∞ was initially chosen for each epoch from Table 3. However, we found it challenging to achieve a good fit to the P Cygni absorption components of all lines with the same value of V_∞ . In general, the value of V_∞ deduced from the C IV line leads to a model in which the extent of the He II 1640 Å and P V 1118-28 Å P Cygni absorption is greater than observed (Fig. 12). The difference is ~ 500 km/s. As mentioned in Section 2, the wind velocity determined from the He II 1640 P Cygni edge is systematically smaller than that derived from C IV (listed in Table 3). A slower wind velocity law (i.e. $\beta > 2$) reduces this discrepancy. However, in the case of N V 1240 Å our models require a faster V_∞ than that derived from C IV, although the measurements of Table 2 give values that are consistent, within the uncertainties, with C IV. Increasing the value of β does not eliminate this inconsistency in the model. Similar discrepancies are observed in some central stars of planetary nebulae (Morisset and Georgiev 2009; Herald et al. 2011; Arrieta et al. 2011). This phenomenon needs further investigation. For the purposes of this paper we used the V_∞ as derived from the C IV 1548-50 Å line and $\beta = 2$.

5.2.3. *Stellar mass and luminosity*

No feature in the spectrum is clearly dependent on the gravity acceleration. This is not surprising given that the continuum forming region extends beyond the photosphere. But the mass of the star, $M \sin i$, i being the orbital inclination, has been estimated from the analysis of the light curve and radial velocity curve to be between 60 and 80 M_\odot . Our modeling shows that at the observed luminosities and mass loss rates, a star with a mass smaller than 90 M_\odot is above the Eddington limit. To keep the star stable, we assume a mass of 90 M_\odot which, within the errors, is consistent with the orbital solution and keeps the stellar photosphere below the Eddington limit. The $\log g$ was adjusted so the mass of the star is

maintained the same for all epochs.

The luminosity at different epochs was determined from the continuum level of the flux calibrated UV spectra. We assume a distance to the SMC of 64 kpc which is an average of the values obtained by Hildich et al. (2005) and North et al. (2010). The reddening was determined by comparing the model and observed spectral energy distribution in the 920 Å - 11500 Å range and using the Cardelli et al. (1989) reddening law. We obtained a good fit with $E(B-V)=0.065\pm0.005$ and $R = A_V/E(B-V) = 3.1$ which was used for all epochs.

5.2.4. Temperature, mass-loss rate and clumping

The temperature and the mass loss rate are the most difficult parameters to determine. The change in the spectrum over the different epochs was so great that one cannot use the same diagnostic feature for the analysis for all epochs. The ever present helium lines are affected by *Star B* in a yet unclear way so we avoided using them. We concentrated on lines which significantly change from epoch to epoch and therefore can safely be assumed to arise in *Star A*. Nitrogen is present as N III, N IV and N V in different epochs and due to this variability we deduce that Nitrogen lines are formed mostly in *Star A*'s wind. We used the N IV 1486] line as a mass loss diagnostic and the N III 1750 Å and 4640 Å lines (when present) were used to constrain the temperature. Although we did not use the helium lines for this analysis, the fits to the He II lines are reasonably good in most of the epochs. He I lines are reasonably fit in 1994 and 2000 epochs but the models underestimate them in 2009. The profile of He I lines is also narrower for the observed V_∞ . This suggests that at least part of the observed He I 5876 Å emission originates in wind-wind interaction region.

It is now well established that the winds of the massive stars are not homogeneous but rather made of clumps, although the true nature of the clumping is not known. The main effect of the clumping in the WR winds is the absence of electron scattering wings of the strong emission lines. Following the same procedure as in Hillier et al. (2003) we used the volume filling factor f prescription. We adjusted f until we fit the red wing of He II 4686 Å line and then check the consistency with the other strong H I + He II lines. The observed electron scattering wings are very weak which restrict the volume filling factor to $f \leq 0.025$. This is an upper limit to f . In some spectra the wings of the lines are even weaker, but smaller values for f might be beyond the validity of the approximations used in the formalism. We used $f=0.025$ for all models for all epochs.

5.2.5. *The individual spectral fits*

Spectrum 1994: Of the four spectra, this one corresponds to the coolest temperature. N III 1750Å blend is clearly seen and we use the ratio N III 1750/N IV 1718Å as a temperature diagnostic. The optical part of the spectrum shows N III 4640 Å line which is also well reproduced. In the low resolution *IUE* spectrum, the observed Fe IV lines in the 1600-1700Å are much weaker than predicted. The mass loss rate was fixed mainly by N IV] 1486 but is consistent with the other UV emission lines. Taking into account the clumping, our derived \dot{M} is in reasonable agreement with that derived in Koenigsberger et al. (1998b) for the same observed spectrum. A likely explanation for this discrepancy is that the model used in that study considered only hydrogen and helium, thus missing the important influence of the line blanketing.

Spectrum 2000: The temperature of the star is low enough to show a measurable N III 4640Å. We used that line to restrict the upper limit of the temperature. The mass loss rate was constrained by N IV] 1486 Å and further checked with the Fe V UV complex. The model also reproduces well the optical He I and He II lines.

Spectrum 2002: The spectrum of this epoch does not include the optical wavelengths. We set the temperature based on the Fe VI/Fe V features observed between 1250 Å and 1400 Å and 1420 Å and 1480 Å respectively. The mass loss rate is derived from N IV] 1486 and the P V 1118-28 Å doublet.

Spectrum 2009: The temperature was limited from below by the absence of N III 4640 Å. This line is present in the previous epochs but is weak in this last spectrum. In addition we used the Fe V/Fe IV UV complex.

The uncertainties in the results obtained from the model fits are difficult to estimate due to the large number of free parameters which are not completely independent. However, the models show that changing $T(\tau_{Ross}=10)$ by more than ~ 2000 K causes changes in the computed spectrum that make it noticeably different from the observations. In an analogous manner, the uncertainty in the mass-loss rate can be estimated to be 30%. The uncertainty in the luminosity due to the uncertainties in the flux calibration and in the S/N of the spectra is $\lesssim 20\%$. The absolute uncertainty in the parameters is much larger due to unclear correlations between them which are difficult to quantify. We minimize these errors by making our models for the different epochs consistent so the differences in the parameter values are expected to reflect real changes in the stellar physics.

5.3. Results

Table 6 summarizes the parameters derived from the models of *Star A* in the epochs 1994, 1999, 2002 and 2009 as well as the model of *Star C*. The comparison between the observations and the calculated spectra are shown in Figs. 11, 12, 13, 14 and 15.

Three different radii are listed in Table 6: 1) R_{10} , which is the radius at which the Rosseland optical depth $\tau_{Ross} = 10$, and it is this reference radius at which the gravity acceleration is $\log g$ and where the temperature T_{10} , is given by the CMFGEN model; 2) R_s , which is the radius at the sonic point, where the optical depth and temperature are, respectively, τ_s and T_s ; we define the photosphere as that region of the star with $r < R_s$ and the wind where $r > R_s$; 3) $R_{2/3}$, which is the radius of the continuum-forming region, where $\tau_{Ross} = 2/3$, and here $T_{eff} = T(R_{2/3})$.

The most outstanding results derived from these models are:

1. The luminosity of *Star A* is higher during the 1994 eruptive event than at later epochs. This is consistent with the results obtained by Drissen et al. (2001) from a spectrum take on 1994 September 21. Their luminosity is even higher than our value for the spectrum obtained on 1994 December 31. The luminosity is lowest in 2000 April, and then rises slightly in 2002 remaining at the same level until 2009. Thus, we are now able to confirm that the 1994 eruption is an event which did not occur at constant luminosity.
2. *Star A*'s mass-loss rate is a factor of ~ 4 larger in 1994 than at later epochs. The larger luminosity most likely plays an important role in driving the larger mass-loss rate.
3. The radius at $\tau_{Ross}=2/3$, $R_{2/3}=124 R_{\odot}$, is larger in 1994 than at any other epoch, and it is very much larger than $R_s=21.5 R_{\odot}$, the radius at the sonic point in 1994. The continuum-forming region is very extended. Fig. 16 shows the temperature structure of the 1994 model where one can also see that due to the larger wind density, the temperature is significantly higher throughout the wind. It is also quite remarkable that the temperature at the sonic point is $T=10^5$ K. This high temperature is due to the fact that radiation is trapped within the extended continuum emitting region.
4. $R_{2/3}$ declines after 1994 reaching $28 R_{\odot}$ in 2009. This value is larger than the size of the observed continuum-emitting region of *Star A* in 1979 ($22\text{--}25 R_{\odot}$; Perrier et al. 2009), consistent with the notion that *Star A* has still not recovered its minimum state of activity. The decrease in $R_{2/3}$ reflects the shrinking size of the continuum forming region as the density drops. Note, however, that $R_s=19.5 R_{\odot}$ in 2009 epoch, indicating that the continuum formation region is still rather extended.

5. The most significant change in R_s occurred in the 2000 epoch, at which time it was larger than during the other epochs. This is consistent with the long-term behavior of the optical light curve which peaked at around the 2000 epoch and with the notion that the long-term activity cycle and the brief eruptions of 1993-1994 seem to be separate phenomena (Koenigsberger et al. 2010).
6. There is a 30% variation in \dot{M} between 2000 and 2002 and it remains relatively constant thereafter. Although it is tempting to suggest a declining trend, the variation lies within the uncertainties of the model results. Hence, we tentatively conclude that \dot{M} is approximately constant over the timescale 2000–2009. This leads to the conclusion that the observed spectral changes during this timescale result primarily from the declining wind density, caused by the increasing wind velocity. Hence, we are now in the possibility of understanding the relation between the flux in N IV] 1486 Å and the terminal wind speed (Fig. 5). Based on the models we can conclude that the reduction of the post-eruption line intensities is caused mainly by the increase of V_∞ . Assuming that V_∞/V_{esc} is constant (Fig. 17) one can conclude that the changes in V_∞ are caused by a decreasing radius of the star (Table 6). The relation between N IV] 1486 Å and the terminal velocity is maintained during the pre-eruption epochs and it follows the same general trend (Koenigsberger et al., 2010) but in the opposite direction. V_∞ decreases while N IV] 1486 Å increases which points to an increase in the stellar radius. This leads us to conclude that the S Dor-type ~ 40 year variability timescale of *Star A* is due to variations in its radius.

The S Dor type variability of *Star A* is similar to that of AG Car (Groh et al. 2009) and S Dor (Lamers 1995). Excluding the 1994 eruption event, the maximum of the optical brightness in HD 5980 was attained between 1996-2000. At that time, the terminal wind velocity and the temperature were lower than in 2009, when the visual brightness was approaching its minimum. In this sense, during its long term variability, *Star A* behaves similarly to AG Car and S Dor. Lamers (1995) explained this variability as a pulsation of 10^{-3} to 10^{-2} of the stellar mass in S Dor, and Groh et al. (2009) reached the same conclusion for AG Car. Lamers (1995) suggested that the larger radius decreases the gravity acceleration and increases the scale height which leads to larger mass loss. He also suggested that the luminosity of the star should be lower during the maximum of the optical brightness due to the work the star must perform to lift the upper layers. In agreement with this prediction we detected a small difference in the luminosity in 2000 (close to maximum) and 2009 (close to minimum) epochs which add weight to the suggestion that S Dor variability of *star A* is caused by a pulsation. The exact physical mechanism causing the pulsation is unclear but now that we have three objects showing similar effects, the question arises as to whether this may be a common phenomenon in this class of objects.

6. The 1994 eruption and the bi-stability jump of a second kind

The results presented in Table 6 indicate that the wind structure of *Star A* in 1994 was significantly different from its wind structure during the other 3 epochs. This difference is best illustrated in Fig. 16 where we plot the temperature structure derived from the spectra of 1994 and 2009. The temperature is higher throughout most of the wind in 1994 than in 2009, even though the observed 1994 spectrum looks cooler. This is a consequence of the higher density in 1994 which makes the wind more optically thick.

The velocity structures are also different, in particular, the relation between the terminal wind velocity, V_∞ and the escape velocity V_{esc} , which is defined as

$$V_{esc} = \left(\frac{GM(1 - \Gamma)}{R_{10}} \right)^{1/2} \quad (4)$$

where M is the stellar mass assumed to be $90 M_\odot$. The ratio between gravity acceleration and the radiation pressure $\Gamma = g_{el}/g_{grav}$ takes into account only the radiation pressure caused by electron scattering (Lamers and Cassinelli, 1999). We calculate V_{esc} using Γ as determined by the CMFGEN model at R_{10} . Fig. 17 shows V_∞ plotted against V_{esc} . The values for the three post-eruption epochs (2000, 2002 and 2009) lie close to a single straight line, the slope of which is ~ 2.3 . The wind during the 1994 epoch is different. In this case, $V_\infty/V_{esc} \sim 1.2$. The velocities obtained by the Drissen et al. (2001) for 1994 September lie along the same relation.

The change in the V_∞/V_{esc} relation together with the cooler effective temperature of the 1994 spectrum are strongly suggestive of a phenomenon associated with the bi-stability jump (Lamers et al. 1995). The bi-stability jump occurs when the temperature in the inner wind decreases to a value at which the ionization fraction of Fe^{2+} increases leading to changes in the line opacities and a changes of the driving force, higher mass loss rate and reduce in V_∞/V_{esc} from ~ 2.6 to 1.3 (Vink et al, 1999). This occurs at $T_{eff} \sim 21000$ K.

This is remarkably similar to what we find for HD 5980. There is, however, a major difference between the cause of the bi-stability jump observed in O and B stars and the phenomenon that our models indicate is occurring in HD 5980. As was shown by Lamers and Cassinelli, (1999) and Vink et al. (1999), the mass loss rate is defined by the force below the sonic point. In the optically thin O and B star's winds the sonic point is above the photosphere, thus the condition in it can be described by the effective temperature. On the other hand, the sonic point of the optically thick wind of HD5980 is located below the pseudo photosphere (Fig. 16). In the 1994 model, the point at which the temperature $T \sim T_{eff} \sim 21000$ K lies at $\sim 6 R_s$ far above the sonic point. Thus, changes in the ionization

structure at a distance of $\sim 6 R_s$ have little effect on the overall wind structure.

In search of an alternative cause of the jump we followed the reasoning of Lamers and Nugis (2002), and Gräfener and Hamman, (2008). These authors showed that the WR winds below the sonic point are driven not by the line force but rather by the radiation pressure due to continuum opacities. We applied that idea to *star A*’s wind. In Table 6 we see that the optical depth of the sonic point $\tau_s > 1$ for all four epochs, indicating that the wind is driven primarily by the continuum force. Lamers and Nugis (2002), and Gräfener and Hamman, (2008) showed that in order to drive a WR-type wind, the continuum opacity (sum of the true continuum opacities and the pseudo continuum of overlapping lines) has to be dominated by one of the bumps in the iron opacity. Gräfener and Hamman, (2008) showed that the required high mass loss rate is obtained only if the temperature at the sonic point is either in the 30-70kK range (“cool” bump) or around 160kK (“hot” bump). Table 6 shows that all of the post eruption models have $T_s \sim 48\text{--}50$ kK, well within the first of these temperature intervals. One can thus expect that at almost constant luminosity the mass loss rate will be almost constant, which is indeed the result from our models (Table 6). During the eruption the luminosity of the star increased. The higher luminosity heated the inner part of the wind changing the opacity contributors from those of the “cool” bump to those of the “hot” bump, thus changing the driving force and therefore the mass loss rate. Our model for 1994 December gives $T_s = 100\text{kK}$ (Table 6). This temperature is too high for the “cool” iron opacity bump but too cool for the “hot” bump at 160kK. Gräfener and Hamman (2008) suggested that winds with T_s in the intermediate temperature range are unstable. We speculate that at the onset of the eruption T_s was high enough and the very dense wind was driven by the high temperature iron bump. As the luminosity decreased, the cooler wind became unstable and it rapidly switched back to the “cool” iron bump driving with T_s around 50 kK.

We suggest that a bi-stability jump of a second kind operates in *Star A*. The sudden change in the wind properties is due to a transition from the “hot” to the “cool” Fe-bump opacity regimes mechanism that was shown by Lamers & Nugis (2002) and Gräfener & Hamann (2008) to be needed to drive the winds of WR stars.

Our models show that the increased luminosity can indeed change T_s , changing the entire wind structure during the eruption. Fig. 16 shows the change in the temperature structure of the wind in the 1994 and 2009 models. In the less dense wind of 2009, the continuum forming region has moved further in and T_{eff} increased. The sonic point is at a similar radius but due to the overall smaller temperature gradient it is significantly cooler. In addition to the changes in the temperature, the value of Γ changes from ~ 0.75 during the eruption to ~ 0.53 afterward. A similar result was found by Smith et al. (2004). These

authors showed that when the star approaches the Eddington limit, the optical depth of the sonic point increases and it moves below the photosphere. The increased luminosity of *star A* moved it closer to the Eddington limit and the wind reacted in a similar manner. Furthermore Gräfener and Hamann (2008) found that the WN stars with SMC chemical composition require $\Gamma > 0.75$ to maintain a high mass loss rate. In addition the Vink et al. (2011) models show a transition from O star wind to WR wind when Γ increases above 0.7. Based on these considerations we can conclude that the wind during the eruption is governed by different forces than the wind in the post eruption epochs. We speculate that during the eruption, the high luminosity heats the inner part of the wind, driving much higher mass loss through the “hot” iron opacity bump. After the eruption the temperature at the sonic point drops making the wind unstable. The mass loss rate drops, which causes further cooling of the sonic point until it reaches the “cool” iron bump where the wind stabilizes again and the star continues its long-term variability but with a restructured wind.

Hence, we suggest that for the dense winds such as those in HD 5980, there exists a second type of bi-stability jump than that proposed by Lamers et al. (1995). It is caused by transition between the “hot” and “cold” iron opacity bump and is correlated mainly with the stellar luminosity rather than with the effective temperature. Smith et al (2004) discussed the position of the sonic point in the typical LBVs. They showed that for the derived parameters of most of the LBVs, the sonic point is located above the photosphere and thus their winds change according to the “classical” bi-stability jump. Here we speculate that the most luminous LBVs, such as *star A*, have optically thick winds with pseudo photospheres above their sonic points even on the hotter side of the S Dor instability strip. Thus their excursion to the cool branch of the strip is caused by a second kind of bi-stability jump related to the changes in their continuum opacities.

7. Conclusions

HD 5980 is a relatively nearby system in which processes involving eruptive phenomena and massive star evolution in binary systems in a low metallicity environment can be studied. In this respect, is important to gain an understanding of the phenomena that it has presented over the past few decades.

In this paper we present the results of the analysis of a collection of UV and optical spectra obtained between 1979 and 2009 and performed CMFGEN model fits to spectra of 1994, 2000, 2002 and 2009. The primary results are as follows: a) The long term S Dor-type variability is associated with changes of the hydrostatic radius. We find that the radius of the eruptor at the sonic point was largest in the year 2000 ($R_s=24.3 R_\odot$), coinciding with

the long-term maximum in the visual light curve. The minimum value in our data set is in 2009 ($R_s=19.6 R_\odot$).

b) The 1994 eruption involved changes in the eruptor’s bolometric luminosity and wind structure. The luminosity was larger by at least 50% with respect to the subsequent epochs and the temperature throughout most of the wind was significantly higher. The latter is a consequence of the very large optical depth which causes photons to be trapped within this wind region. At the same time, the velocity structure was one in which the relationship between the terminal wind velocity and the escape velocity $V_\infty/V_{esc} \sim 1.2$, contrary to other epochs in which this ratio was ~ 2.3 . c) the emission-line strength, the wind velocity and the continuum luminosity underwent correlated variations in the sense that a decreasing V_∞ was associated with increasing emission line and continuum levels. These correlations can be understood in the context of the increasing size of the hydrostatic stellar radius. d) The spectrum of the third star in the system (*Star C*) is well-fit by a $T_{eff}=32$ K model atmosphere with SMC chemical abundances. The abundances of the eruptor, *Star A*, show He and N enhancements, roughly consistent with the CNO cycle equilibrium values. A similar composition was obtained by Groh et al. (2009) for AG Car and Hillier et al. (2001) for η Car.

For all epochs, the wind of the erupting star is optically thick at the sonic point and is thus driven mainly by the continuum opacity. We speculate that the wind switches between two stable regimes driven by the “hot” (during the eruption) and the “cool” (post-eruption) iron opacity bumps as defined by Lamers & Nugis (2002) and Gräfener and Hamann (2008), and thus the wind may undergo a bi-stability jump of a different nature from that which occurs in OB-stars.

8. Acknowledgements

We thank Alfredo Díaz and Ulises Amaya for computing assistance. This research was supported under UNAM/DGAPA/PAPIIT grants IN106798, IN123309 and CONACYT grants 48929 and 83016. LNG acknowledges the support from CONACyT grant 141530. RHB acknowledges partial support from ULS DIULS grant, and DJH acknowledges support from grant HST-GO-11623.01-A and HST-GO-11756.01. The HST is operated by the STSCI, under contract with AURA.

REFERENCES

- Arrieta, A., Hillier, D. J., Morisset, C., Georgiev, L., Stasinska, G., 2011, in preparation
- Barbá, R. H. & Niemela, V. S. 1994,
- Barba, R. H., Niemela, V. S., Baume, G., & Vazquez, R. A. 1995, *ApJ*, 446, L23
- Barba, R. H., Morrell, N. I.; Niemela, V. S. et al., 1996, *Revista Mexicana de Astronomia y Astrofisica Conference Series*, 5, 85
- Barbá, R. H., Niemela, V. S., Morrell, N. I. 1997, “Luminous Blue Variables: Massive stars in Transition”, ed. A. Nota & H. Lamers, *ASP Conf. Ser.* 120, 238.
- Breysacher, J. 1997, *Luminous Blue Variables: Massive Stars in Transition*, *ASP Conf. Ser.* 120, ed. A. Nota & H. Lamers, 227
- Breysacher, J., Moffat, A. F. J. & Niemela, V. 1982, *ApJ*, 257, 116
- Breysacher, J., & Perrier, C. 1980, *A&A*, 90, 207
- Cardelli, J. A., Clayton, G. C., & Mathis, J. S. 1989, *ApJ*, 345, 245
- Colina, L., Bohlin, F. & Castelli, F. 1996, *Instrument Science Report CAL/SCS-008*
- Crowther, P. A., Hillier, D. J., Evans, C. J., Fullerton, A. W., De Marco, O., & Willis, A. J. 2002, *ApJ*, 579, 774
- Drissen, L., Crowther, P. A., Smith, L. J., Robert, C., Roy, J.-R., & Hillier, D. J. 2001, *ApJ* 545, 484.
- Dufau, S., Ruiz, M., T., 2002, private communication.
- Dufour, R. J. 1984, *Structure and Evolution of the Magellanic Clouds*, 108, 353
- Dwarkadas, V. V. 2011, *MNRAS*, 412, 1639
- Eenens, P. R. J. & Williams, P. M. 1994, *MNRAS*, 269, 1082.
- Foellmi, C., et al. 2008, *Rev. Mexicana Astron. Astrofis.*, 44, 3
- Georgiev, L. N., & Koenigsberger, G. 2004, *A&A*, 423, 267
- Gräfener, G., & Hamann, W.-R. 2008, *A&A*, 482, 945
- Grevesse, N., Asplund, M., & Sauval, A. J. 2007, *Space Sci. Rev.*, 130, 105
- Groh, J. H., Hillier, D. J., Damineli, A., et al. 2009, *ApJ*, 698, 1698

- Guzik, J. A., Cox, A. N., & Despain, K. M. 2005, *The Fate of the Most Massive Stars*, 332, 263
- Heydari-Malayeri, M., Rauw, G., Esslinger, O., & Beuzit, J.-L. 1997, *A&A*, 322, 554
- Herald, J., Bianchi, L., 2011, *MNRAS*, submitted.
- Hilditch, R. W., Howarth, I. D., & Harries, T. J. 2005, *MNRAS*, 357, 304
- Hillier, D.J., Miller,D, 1998, *ApJ*, 496,407
- Hillier, D. J., Lanz, T., Heap, S. R., Hubeny, I., Smith, L. J., Evans, C. J., Lennon, D. J., & Bouret, J. C. 2003, *ApJ*, 588, 1039
- Hunter, I.; Dufton, P. L.; Smartt, S. J.; Ryans, R. S. I.; Evans, C. J.; Lennon, D. J.; Trundle, C.; Hubeny, I.; Lanz, T. 2007, *A&A*, 466, 277
- Jones, A., & Sterken, C. 1997, *Journal of Astronomical Data*, 3, 3
- Kashi, A. & Soker, N., 2010, *ApJ*, 723, 602.
- Koenigsberger, G. 2004, *Rev. Mexicana Astron. Astrofis.*, 40, 107
- Koenigsberger, G., Moffat, A.F.J., & Auer, L. H. 1987, *ApJL*, 322, L41.
- Koenigsberger, G., Moffat et al. 1994, *ApJ*, 436, 301.
- Koenigsberger, G., Guinan, E., Auer, L., & Georgiev, L. 1995, *ApJ*, 452, L107
- Koenigsberger, Shore, Guinan, Auer, 1996, *RMAACS*, 5, 92.
- Koenigsberger,G., Auer,L.H., Georgiev,L. and Guinan, E. 1998, *ApJ*, 496,934.
- Koenigsberger, G., Pena, M., Schmutz, W., & Ayala, S. 1998b, *ApJ*, 499, 889
- Koenigsberger, G., Georgiev, L., Barbá, R., Tzvetanov, Z., Walborn, N. R., Niemela, V. S., Morrell, N., & Schulte-Ladbeck, R. 2000, *ApJ*, 542, 428
- Koenigsberger, G., Georgiev, Leonid; Peimbert, Manuel; Walborn, Nolan R.; Barb, Rodolfo; Niemela, Virpi S.; Morrell, Nidia; Tsvetanov, Zlatan; Schulte-Ladbeck, Regina 2001, *AJ*, 121, 267
- Koenigsberger, G., Kurucz, R., Georgiev, L. 2002, *ApJ*, 581, 598.
- Koenigsberger, G., Fullerton, A., Massa, D. & Auer, L.H. 2006, *AJ*, 132, 1527.
- Koenigsberger, G., Georgiev, L., Hillier, D.J., Morrell, N., Barbá, R., Gamen, R. 2010, *AJ*, 139, 2600

- Kudritzki, R.-P., Lennon, D. J., & Puls, J. 1995, *Science with the VLT*, 246
- Lamers, H. J. G. L. M. 1995, *IAU Colloq. 155: Astrophysical Applications of Stellar Pulsation*, 83, 176
- Lamers, H. J. G. L. M., & Cassinelli, J. P. 1999, *Introduction to Stellar Winds*, Cambridge, UK: Cambridge University Press, June 1999.,
- Lamers, H. J. G. L. M., Snow, T. P., & Lindholm, D. M. 1995, *ApJ*, 455, 269
- Lamers, H. J. G. L. M., & Nugis, T. 2002, *A&A*, 395, L1
- Maíz-Apellaniz, J. & Bohlin, R.C. 2005, *Space Telescope Science Institute, Instrument Science Report STIS 2005-01*
- Moffat, A. F. J., Marchenko, S. V.; Bartzakos, P.; Niemela, V. S.; Cerruti, M. A.; Magalhaes, A. M.; Balona, L.; St-Louis, N.; Seggewiss, W.; Lamontagne, R. 1998, *ApJ*, 497, 896
- Morisset, C., & Georgiev, L. 2009, *A&A*, 507, 1517
- Nichols, J. S. & Linsky, J. L. 1996, *AJ*, 111, 517.
- Niemela, V.S., 1988, *ASPCS* 1, 381.
- North, P., Gauderon, R., Barblan, F., & Royer, F. 2010, *A&A*, 520, A74
- Nugis, T., & Lamers, H. J. G. L. M. 2002, *A&A*, 389, 162
- Owocki, S., & van Marle, A. J. 2008, *IAU Symposium*, 250, 71
- Peimbert, M., Peimbert, A., & Ruiz, M. T. 2000, *ApJ*, 541, 688
- Perez, M. 1992, *NASA IUE Newsletter* 48, 76.
- Perrier, C., Breysacher, J., & Rauw, G. 2009, *A&A*, 503, 963.
- Pojmanski, G. 2002, *Acta Astronomica*, 52, 397
- Prinja, R.K., Barlow, M.J., & Howarth, I.D. 1990, *Apj*, 361, 607
- Schmutz, W., Hamann, W.-R., & Wessolowski, U. 1989, *A&A*, 210, 236
- Schweickhardt, J. 2000, *PhD Thesis*, Ruprecht-Karls-Universität, Heidelberg.
- Smith, N., Vink, J. S., & de Koter, A. 2004, *ApJ*, 615, 475
- Smith, N. 2008, *IAU Symposium*, 250, 193

- Sterken, C. & Breysacher, J. 1997, *A&A*, 328, 269.
- van Marle, A. J., Langer, N., & García-Segura, G. 2007, *A&A*, 469, 941
- Vink, J. S., de Koter, A., & Lamers, H. J. G. L. M. 1999, *A&A*, 350, 181
- Vink, J. S., Muijres, L. E., Anthonisse, B., de Koter, A., Graefener, G., & Langer, N. 2011, [arXiv:1105.0556](#)

Table 1. High dispersion spectra

Spectrum	HJD ¹	Phase	FES mag	HeII _{edge} ²	NV _{sat} ³	F(N IV)] ⁴	F(NIII) ⁴	F(1850Å) ⁵
4277	43921.1	0.57	11.68	-2770	-2800	< 1.	1.0	1.47
4345	43928.6	0.91	11.69	-2620	-2760	< 1.	<1	1.53
4958	43981.0	0.68	11.72	-2800	-2050	< 1.	<1	1.43
	-2790
11175	44632.3	0.48	11.61	-2920	-2610	2.8	2.7	1.58
11190	44634.6	0.60	11.63	-2920	-2540	<1.3	<1	1.64
15072	44869.5	0.80	11.62	-2740	-2450	1.9:	<1	1.61
15080	44870.5	0.85	11.57	-2730	-2130	0.7:	1.5	1.28
	-2650
37759	47867.2	0.39	11.36	-2520	-2210	11.2	1.	1.59
	-2080 ⁸
37768	47868.2	0.44	11.27	-2550	-2050	10.7	<1	1.62
	-1890 ⁸
37781	47870.2	0.55	11.27	-2040	-1750	11.7	<1	1.86
37788	47871.4	0.61	11.25	-2000	-1950	14.3	0.2	1.85
42446	48511.5	0.83	11.41	-1900	-1980	12.5	<1	1.86
42470	48515.6	0.05	11.35	-1700	-1800	16.9	<1	1.82
42694	48541.4	0.39	11.55	-2650	-2450	13.2	1.	1.73
42702	48542.4	0.44	11.50	-2480	-2340	11.1	2.	1.86
42711	48543.4	0.49	11.27	-2480	-2210	14.5	1.4	1.93
42721	48544.4	0.54	11.33	-2450	-2180 ⁶	17.8	<1	1.95
52888	49680.5	0.51	11.37	-420	...	7.4	18.8	3.32
53036 ¹⁰	49697.5	0.39	...	-370	...	14.0:	39.1:	1.96::
53129 ¹⁰	49706.5	0.86	...	-470	...	6.9:	34.6:	1.75::
53216 ¹⁰	49716.5	0.38	...	-370	-1680	23.9	57.0	2.55:
53226 ¹⁰	49717.5	0.43	11.12 ⁷	-370	-1730	21.9	58.1	2.55:
54064	49784.1	0.89	...	-1100	-2010	38.8	39.3	2.50
54490	49831.0	0.32	11.96	-800 ⁸	...	43.6	35.9	2.65
	-1900	-1660
54671	49851.0	0.36	11.98	-810 ⁸	-950:	49.0	35.7	2.49
	-2000	-1900

Table 1—Continued

Spectrum	HJD ¹	Phase	FES mag	HeII _{edge} ²	NV _{sat} ³	F(N IV)] ⁴	F(NIII) ⁴	F(1850Å) ⁵
54727	49859.9	0.82	11.96	-1100 ⁸	-900	37.0	31.6	2.81
	-2400	-2300
55315	49916.8	0.78	11.27	-1100 ⁸	-800:	35.9	20.1	2.55
	-2530	-2150
55380	49928.8	0.40	11.34	-900 ⁸	-1130	38.2	19.2	2.36
	-2230	-2400
55394	49930.8	0.507	11.22	-900 ⁸	-900:	38.6	18.6	2.38
	-2380	-2180
55932	49975.6	0.83	11.22	-1200 ⁸	-1000	31.9	14.7	2.43
	-2620	-2400:
55955	49978.7	0.99	11.37	-1200 ⁸	-880:	31.9	14.4	1.98
	-2530	-2330
56017	49986.6	0.40	11.31	-2670	-2560	37.4	14.4	2.15
56188	50033.5	0.83	...	-1400	-1850	29.0	10.6	2.29
56205	50036.4	0.99	...	-1500	-1000:	31.9	8.2	1.76
	-2160
56223	50045.2	0.43	...	-2530	-2500	30.7	7.1	2.15
1070	51304.8	0.83	...	-1770:	-1600	24.9	0.8	2.08
	-2050
3070	51308.9	0.05	...	-1380	-1570	25.0	0.4	1.68
4070	51310.8	0.15	...	-1350	-1670 ⁸	25.0	0.6	2.15
5070	51314.9	0.36	...	-2500	-1630	23.6	0.5	1.67
	-2130 ⁹
6070	51315.8	0.40	...	-2140	-1650	26.4	0.2	1.85
	-2140
2070	51655.1	0.00	...	-1500	-1830 ⁸	17.9	0.9	1.68
7070	52386.6	0.99	¹¹	-1860	-2100	12.2
8070	55083.9	0.99	11.6 ¹²	-2260	-2460	7.0	<0.2	1.50
	-2610

¹Heliocentric Julian Date -2400000

²ocation where P Cyg absorption intersects the continuum level in km/s. Corrected for an adopted SMC systemic velocity of +150 km/s

³Maximum extent of the plateau (“flat” region) of P Cyg absorption in km/s; two values in this column indicate the presence of a second plateau at a different intensity level. Corrected for an adopted SMC systemic velocity of +150 km/s

⁴Integrated un-dereddened absolute flux in units of 10^{-12} ergs/cm²-s

⁵Un-dereddened absolute flux in units of 10^{-12} ergs/cm²-s-Å

⁶The absorption is not flat, but contains considerable structure

⁷Visual magnitude from Koenigsberger et al. 1998b

⁸Maximum extent of “plateau”

⁹Speed of what may be interpreted as a short plateau; absorption continues to rise gradually out -3100 km/s

¹⁰Flux calibration problem

¹¹Visual magnitude of 11.3 for this same epoch but out of eclipse was provided by S. Dufau & M.T. Ruiz, Private Communication, (2002)

¹²All Sky Automated Survey (ASAS) (Pojmanski, 2002) value obtained ~ 3 hours earlier

Table 2. Low resolution IUE spectra

SWP	HJD ¹	Phase	FES mag	F(N IV)] ²	F(NIII) ²	F(1850Å) ³
1598	43650.5	0.53	11.72	1.8	6.52	1.61
14112	44754.4	0.82	11.61	1.8	2.8	1.73
14135	44756.2	0.92	11.63	5.1	0.7	1.67
14166	44758.8	0.05	11.56	4.6	1.6	1.68
29633	46743.7	0.07	11.42	5.3	0	1.69
29673	46748.9	0.34	11.59	8.9	2	1.35
29674	46748.9	0.35	11.57	7.9	2	1.39
29681	46749.7	0.39	11.49	6.1	2	1.52
29690	46750.8	0.45	11.44	14.7	2	1.68
29693	46750.9	0.45	11.45	8.2	2	1.75
29699	46751.8	0.51	11.41	8.2	0	1.76
29702	46751.9	0.51	11.39	5.0	1	1.75
29705	46752.7	0.54	11.41	7.7	2	1.77
29708	46752.8	0.55	11.39	5.3	1.5	1.76
29736	46757.9	0.81	11.37	5.9	2	1.67
29743	46758.7	0.85	11.40	7.3	2	1.69
37760	47867.5	0.39	11.30	11.7	2.0	1.81
37769	47868.5	0.44	11.25	12.8	1	1.89
37782	47870.5	0.56	11.22	14.0	1	1.93
37789	47871.5	0.61	11.20	14.3	1	1.96
37790	47871.5	0.61	11.37	18.6	3	1.91
42445	48511.5	0.83	11.26	18.7	0.9	1.99
42469	48515.5	0.04	11.43	16.9	0.5	1.82
42693	48541.4	0.38	12.00	12.9	1	1.73
42701	48542.4	0.44	11.39	13.7	2	1.98
42703	48542.7	0.45	11.49	17.2	0.4	2.01
42710	48543.4	0.49	11.27	18.3	2.8	2.06
42720	48544.4	0.54	11.26	14.0	1.	2.04
42722	48544.7	0.55	11.33	16.1	1.7	2.09
52824	49674.9	0.22	10.11	4.0	26.5	3.50
52889	49680.6	0.52	10.19	1.	27.2	3.50

Table 2—Continued

SWP	HJD ¹	Phase	FES mag	F(N IV)] ²	F(NIII) ²	F(1850Å) ³
52922	49684.8	0.73	10.10	4	33.6	3.10
52956	49688.6	0.93	10.22	0.8	29.3	3.05
52967	49689.7	0.99	...	10.8	37.4	3.17
52975	49690.7	0.04	...	12.1	38.3	3.08
52992	49692.7	0.14	10.54	12.0	41.8	2.74
53035	49697.2	0.38	...	23.1	42.6	2.65
53037	49697.6	0.40	...	15.4	44.1	2.60
53061	49702.6	0.66	...	17.1	52.3	2.65
53128	49706.3	0.85	...	18.6	45.0	2.72
53164	49709.9	0.03	...	18.1	45.8	2.65
53186	49712.6	0.18	...	30.7	51.5	2.80
53187	49712.7	0.18	...	31.1	53.3	2.84
53218	49716.6	0.39	...	34.6	56.2	2.90
53230	49717.8	0.44	...	36.5	59.8	3.12
54485	49830.3	0.28	...	45.8	37.1	2.89
54486	49830.5	0.29	...	40.2	37.7	2.94
54491	49831.2	0.33	...	43.9	38.2	2.65
54533	49836.3	0.59	...	39.8	38.3	3.24
54534	49836.3	0.59	...	43.3	42.7	3.30
54535	49836.3	0.59	...	43.4	41.9	3.23
54664	49850.3	0.32	...	41.9	38.6	2.62
54665	49850.4	0.33	...	42.1	38.1	2.68
54666	49850.4	0.33	...	46.4	36.1	2.70
54670	49850.8	0.35	...	47.4	39.5	2.61
54708	49857.4	0.69	...	44.0	37.8	2.85
54709	49857.4	0.69	...	40.4	37.2	2.93
54728	49860.1	0.83	...	45.5	30.1	2.93
54758	49864.1	0.04	...	37.7	34.0	2.53
54759	49864.2	0.04	...	35.1	34.4	2.37
54760	49864.2	0.04	...	32.6	37.8	2.26
55111	49894.1	0.59	10.94	41.6	27.0	2.60

Table 2—Continued

SWP	HJD ¹	Phase	FES mag	F(N IV)] ²	F(NIII) ²	F(1850Å) ³
55112	49894.1	0.60	10.21	45.3	29.5	2.65
55314	49916.7	0.77	11.27	39.3	20.4	2.69
55340	49921.0	0.99	...	41.2	23.8	2.33
55381	49928.9	0.40	11.30	42.0	20.9	2.38
55382	49928.9	0.51	...	40.2	21.6	2.48
55382	49928.9	0.51	...	40.2	21.6	2.48
55395	49930.9	0.51	11.19	42.5	24.1	2.60
55396	49930.9	0.51	11.25	40.3	22.1	2.55
55461	49939.9	0.97	11.33	43.7	24.2	2.17
55462	49939.9	0.98	...	39.0	18.3	2.13
55931	49975.5	0.82	...	45.5	13.0	2.48
55933	49975.8	0.84	...	40.4	15.3	2.40
55954	49978.8	0.99	...	41.9	19.0	1.96
55956	49978.8	0.99	...	36.8	14.9	2.14
55957	49978.8	0.00	...	37.1	14.6	2.07
55958	49978.9	0.00	...	35.5	18.6	2.08
55976	49981.8	0.15	...	33.0	15.8	2.40
55977	49981.9	0.15	...	39.2	18.1	2.48
56005	49985.0	0.32	...	42.7	17.3	2.03
56006	49985.1	0.33	...	40.0	13.9	2.20
56013	49985.9	0.36	...	37.2	16.3	2.17
56014	49985.9	0.36	...	36.7	13.0	2.08
56015	49985.9	0.36	...	32.0	13.2	2.13
56018	49986.7	0.40	...	42.2	15.3	2.34
56033	49990.8	0.62	...	38.7	15.3	2.48
56034	49990.9	0.62	...	31.7	14.3	2.47

¹Heliocentric Julian Date -2400000

²Integrated un-dereddened absolute flux in units of 10^{-12} ergs/cm²-s

³Un-dereddened absolute flux in units of 10^{-12} ergs/cm²-s-Å

^dVisual magnitude from Koenigsberger et al. 1998b

Table 3. Estimated wind speeds

Year				V_{edge} (HeII)
	<i>Star A</i>	<i>Star B</i>	<i>Star C</i>	<i>Star A</i>
1979	−2670 ¹	...	−1760	−2560
1991	−2000 ¹	−2320	−1740	−1870
1993.7	−1610 ²
1994.90	−690 ³
1994.94	−810 ³
1994.97	−860 ³
1994.98	−1100 ³
1995.00	−1300 ³
1999	−1720 ¹	−2300	−1740	−1500
2000	−2000 ¹	...	−1780	−1680
2002	−2210 ¹	...	−1780	−2100
2009	−2440 ¹	...	−1760	−2260

¹From V_{black} C IV

²From P V, *FUSE*, Koenigsberger et al. 2006

³From Al III, Koenigsberger et al. 1998a

Table 4. Ions and number of levels treated in the model

Elements	I	II	III	IV	V	VI	VII	VIII	IX
H	20/30								
He	27/39	13/30							
C		40/92	51/84	59/64					
N		45/85	41/82	44/76	41/49				
O		54/123	88/170	38/78	32/56	25/31			
Ne		42/242	40/182	53/355	37/166	36/202			
Al			21/65						
Si			20/34	22/33					
P				36/178	12/62				
S			13/28	51/142	31/98	28/58			
Cl				40/129	26/80	18/44	17/28		
Ar			10/36	31/105	38/99				
Ca				43/378	73/613	47/108	48/288	45/296	39/162
Cr			30/145	29/234	30/223	30/215			
Mn				39/464	16/80	23/181	20/203		
Fe			104/1433	100/1000	139/1000	44/433	29/153		
Ni				115/1000	152/1000	62/1000	37/308	34/325	34/363

Table 5. Chemical composition of *Star A* compared to other objects

Element	<i>Star A</i> ^a	<i>Star C</i> ^a	SMC ^b	NGC346 ^c	AG Car ^e	Sun ^d
H	11.304	11.853	11.868	11.868
He	11.902	11.455	...	11.381	12.097	11.397
C	7.484	8.233	8.694	9.334
N	9.000	7.999	7.526	7.521	10.161	8.791
O	6.176	9.057	9.224	9.219	8.679	9.729
Ne	8.241	8.542	8.474	8.470	...	9.010
Na	6.538	6.839	7.396
Mg	7.811	8.111	8.780
Al	6.747	7.049	8.056	7.666
Si	7.844	8.146	9.123	8.823
P	5.787	6.086	6.716
S	7.562	7.863	7.966	7.961	...	8.511
Cl	5.896	6.196	6.914
Ar	6.009	7.310	7.291	7.286	...	7.646
Ca	6.809	5.865	7.778
Ti	5.516	7.090	6.445
Cr	6.230	6.531	7.221
Mn	5.975	6.274	6.995
Fe	8.134	8.436	9.442	9.062
Ni	6.865	7.164	7.863

^aThis paper;

^bHunter et al. 2007;

^cPeimbert et al. 2000;

^dGrevesse et al.2007;

^eGroh et al., 2009;

Table 6. Model Fit Results

Parameter	Sept. 1994 ^a	Dec. 1994 ^b	Dec. 1994 ^c	2000 ^c	2002 ^c	2009 ^c	starC ^c
JD - 240000.0	...	49716.6	49716.6	51655.1	52386.6	55083.9	...
V [mag] (system)	...	11.12	11.12 ^b	11.3	11.6
R ₁₀ [R_{\odot}]	...	48 ^d	28	20.4	21	19.3	23.5
R _s [R_{\odot}]	21.5	24.3	21.2	19.6	25.0
R _{2/3} [R_{\odot}]	280	...	124	34	32	28	24.2
τ_s	25.8	4.7	3.7	1.8	0.005
T _{eff} [kK]	23	37.3	40	43	32
T _* [kK]	23	35.5 ^d	47	48	50	47	33
T _s [kK]	100	57	58	60	27
\dot{M}/\sqrt{f} [$10^{-5}M_{\odot}/yr$]	80	100	111	35	25	23	0.06
Log(L/L _{\odot})	7.05	6.48	6.57	6.30	6.39	6.39	5.77
V _{∞} [km/s]	500	600	750	2000	2200	2440	1800
V _{esc} [km/s]	464	...	642	832	895	932	...
Γ	0.75 ^e	...	0.75	0.53	0.53	0.53	...

^aDrissen et al. 2001;

^bKoenigsberger et al. 1998b;

^cThis paper;

^d“Core” radius, R_{*}, and corresponding temperature; in Koenigsberger et al. (1998b), R_{*} is the inner boundary of the model atmosphere, where the expansion velocity is negligible

^eAdopted value same as in 1994 model.

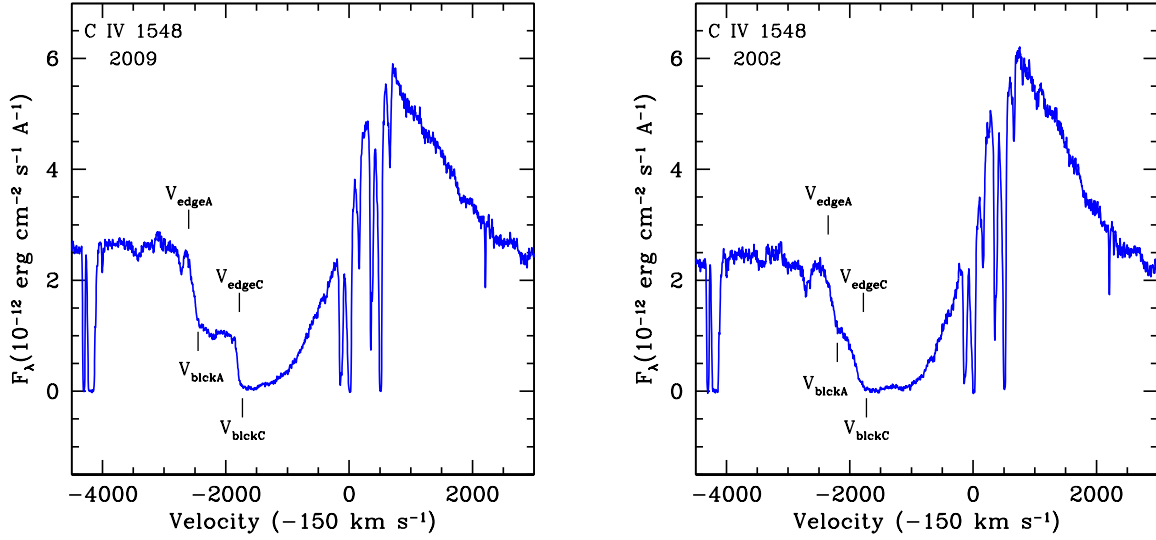


Fig. 1.— The C IV 1548-1550 Å P Cygni doublet observed in 2009 (left) and 2002 (right) on a velocity scale centered on the 1548 Å laboratory wavelength corrected for the SMC motion (+150 km/s).

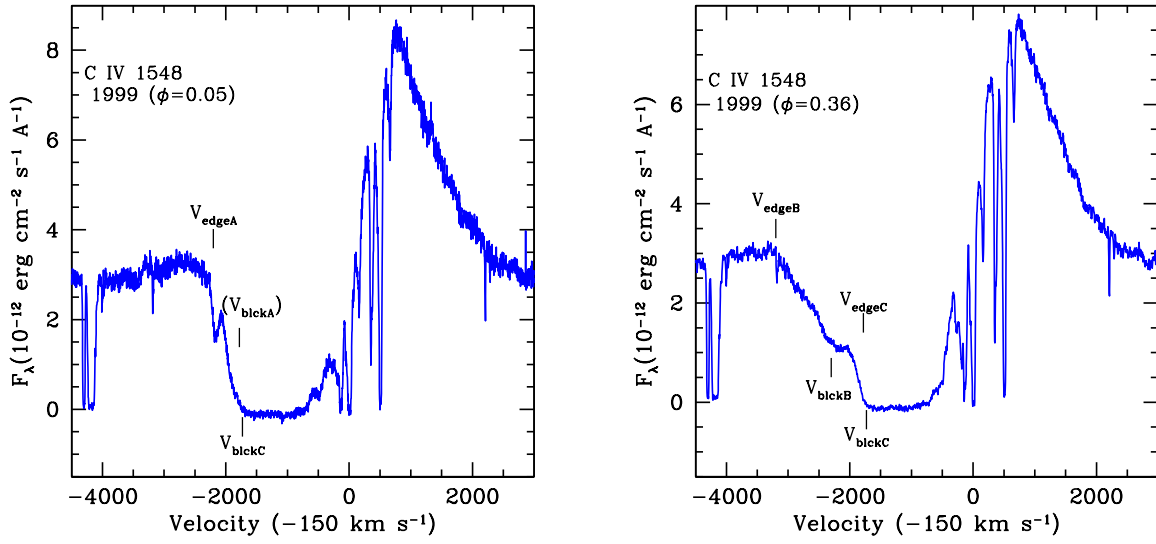


Fig. 2.— The C IV 1548-1550 Å P Cygni doublet observed in 1999 at orbital phases 0.05 (left) and 0.36 (right), the latter corresponding to the eclipse when *Star B* is “in front”. The velocity scale is centered on the 1548 Å laboratory wavelength corrected for the SMC motion (+150 km/s). The large difference of 950 km/s between V_{edgeB} and V_{blackB} in right panel indicates a large amount of “turbulence”.

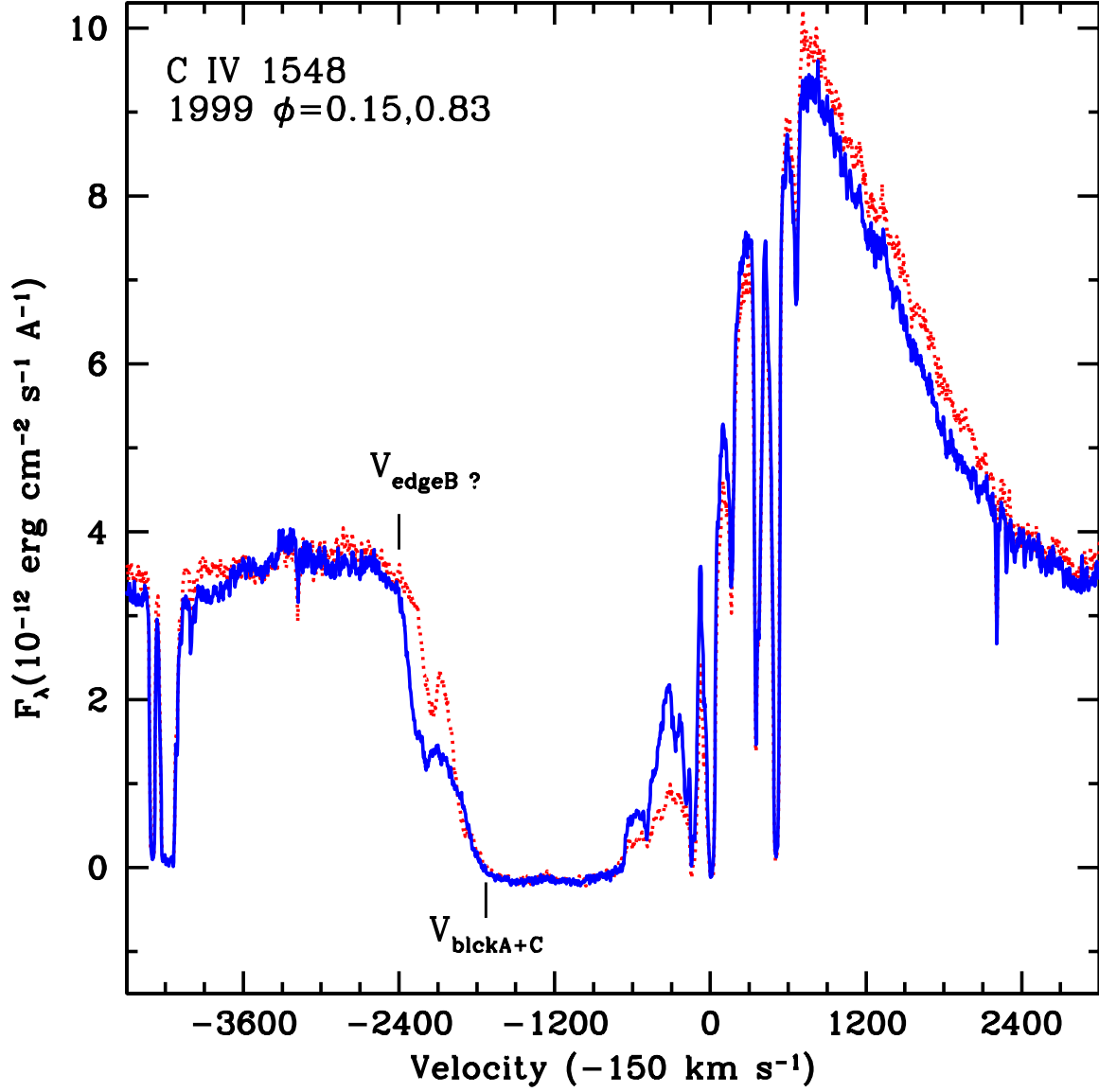


Fig. 3.— The C IV 1548/1550 P Cygni doublet observed in 1999 at orbital phases 0.15 (dotted line) and 0.83. These phases correspond to the largest projected orbital motion of the stars in the 19.3d binary. The “turbulet” edge velocity of -3100 km/s seen at $\phi=0.36$ is absent, possibly due to the wind-wind interaction region. The velocity scale is centered on the 1548 \AA laboratory wavelength corrected for the SMC motion ($+150 \text{ km/s}$).

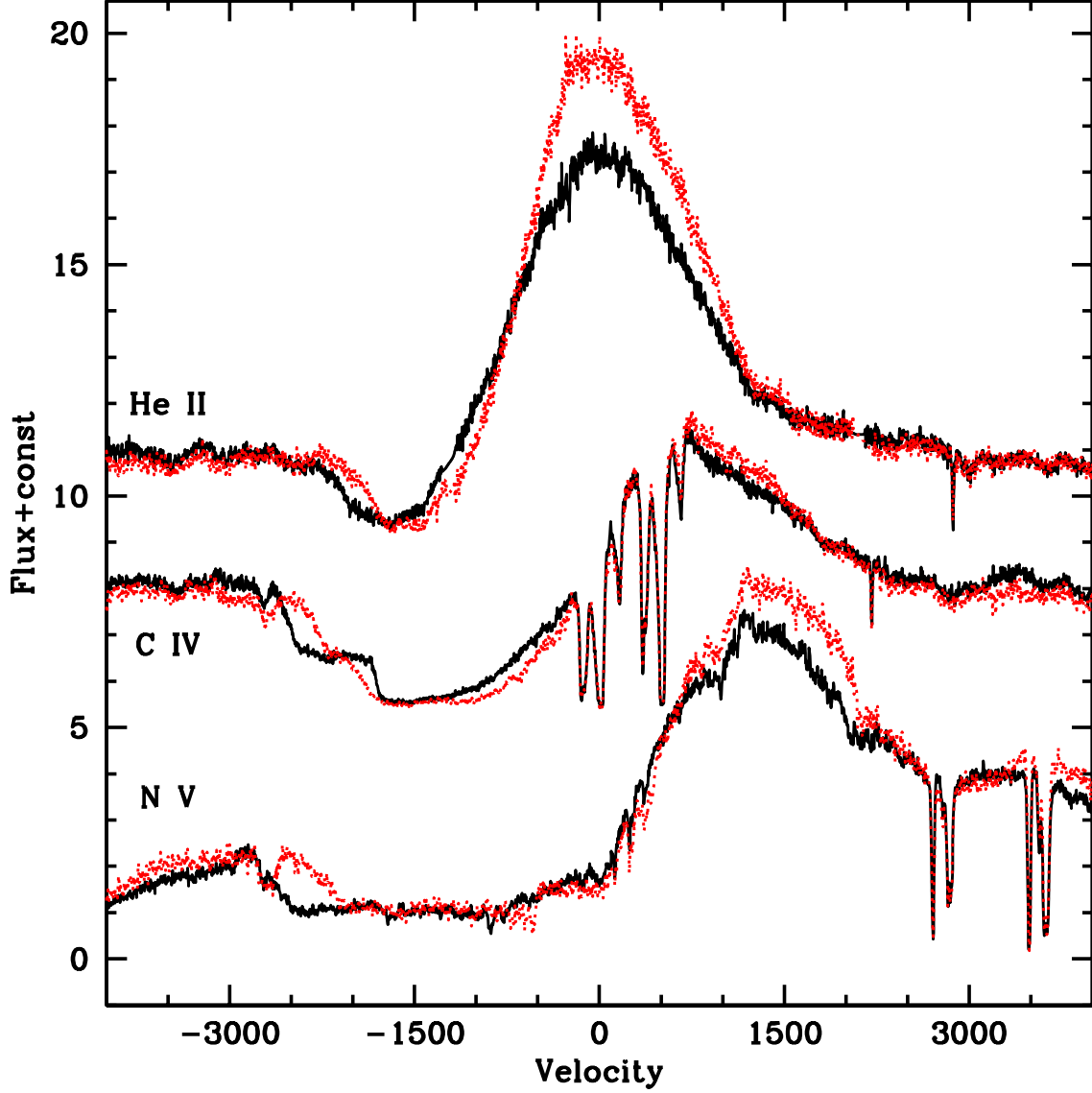


Fig. 4.— Montage of the N V, C IV and He II P Cygni profiles in the *HST/STIS* spectra obtained in 2002 (dots) and 2009. Both spectra correspond to the same orbital phase $\phi = 0.99$. The most striking differences are the strength of the emission line and the extent of the absorption component. Note the “step”-like shape of the C IV absorption component in 2009 due to the contribution from *Star C* (–1760 km/s) and *Star A* (–2440 km/s). Velocity scale is centered on the laboratory wavelengths of NV1238.821, C IV 1548.187 and He II 1640.47, with a correction of –150 km/s to account for the relative SMC motion.

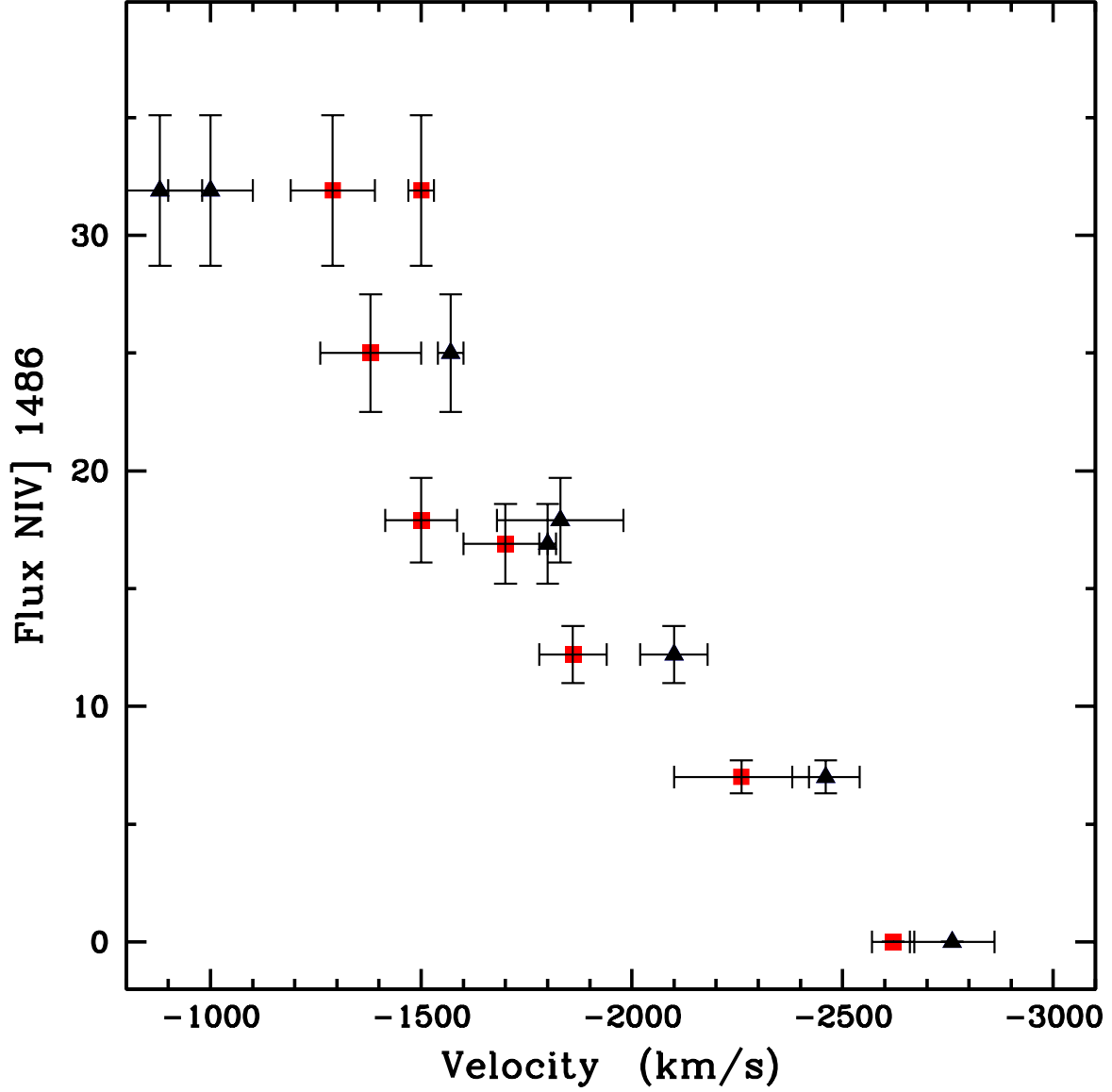


Fig. 5.— Line strength *vs.* wind velocity correlation. The N IV] 1486 Å emission-line flux plotted against the wind velocity derived from P Cygni absorption profiles. Only data from spectra obtained around $\phi = 0.00$ are plotted. Squares correspond to V_{edge} of He II 1640 Å and triangles correspond to the saturation portion of N V 1238. Error bars in velocity correspond to estimated uncertainties in each individual measurement while the flux uncertainty is estimated at 10%.

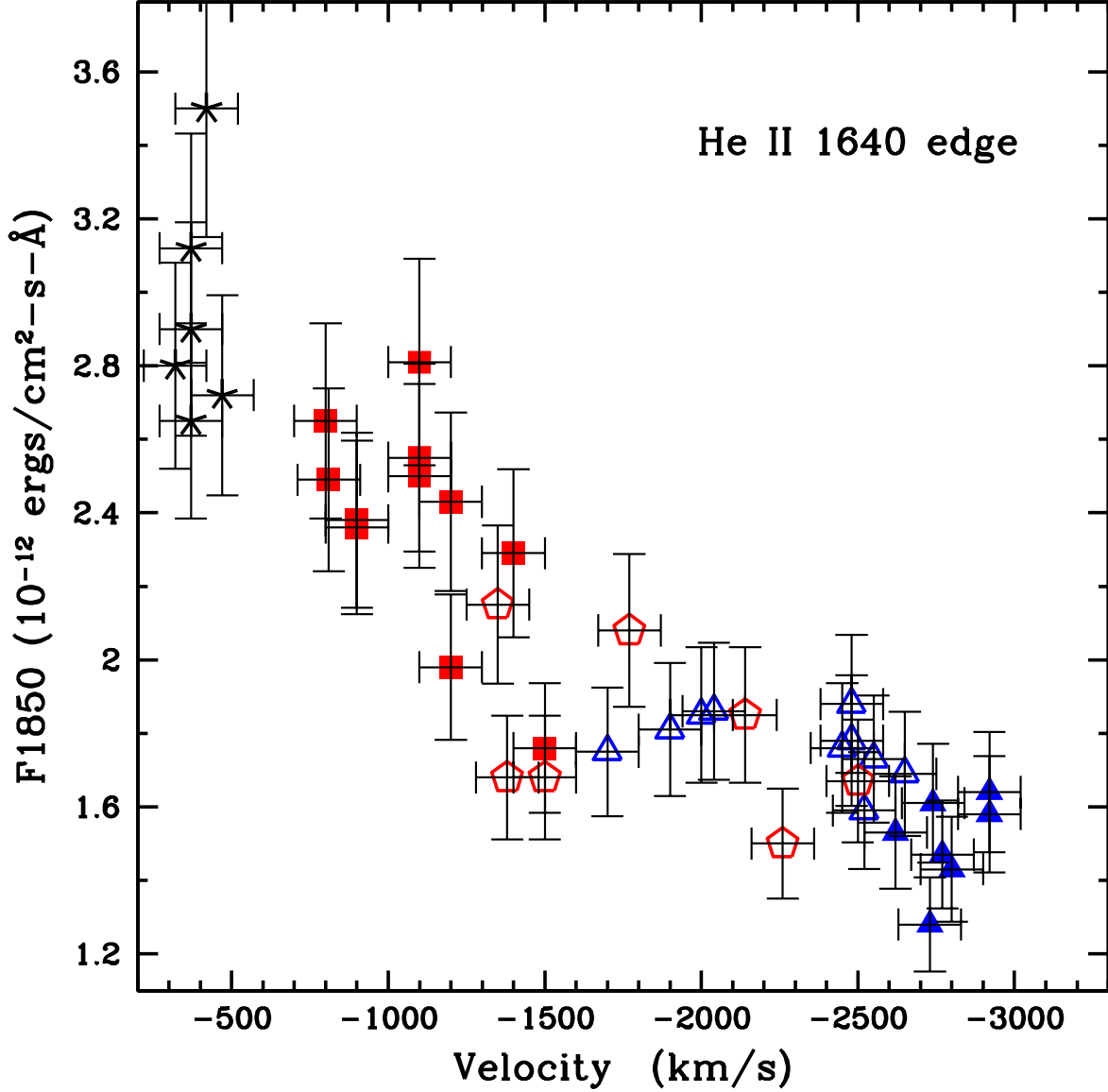


Fig. 6.— Continuum intensity *vs.* wind velocity correlation. The UV continuum flux level, F_{1850} , plotted against the wind velocity derived from V_{edge} of He II 1640. Symbols indicate: filled triangles – 1979–1981; open squares – 1986; open triangles – 1989–1991; stars – 1994; filled squares – 1995; and pentagons – 1999–2009. For 1994, we use values of F_{1850} measured on the low dispersion spectra.

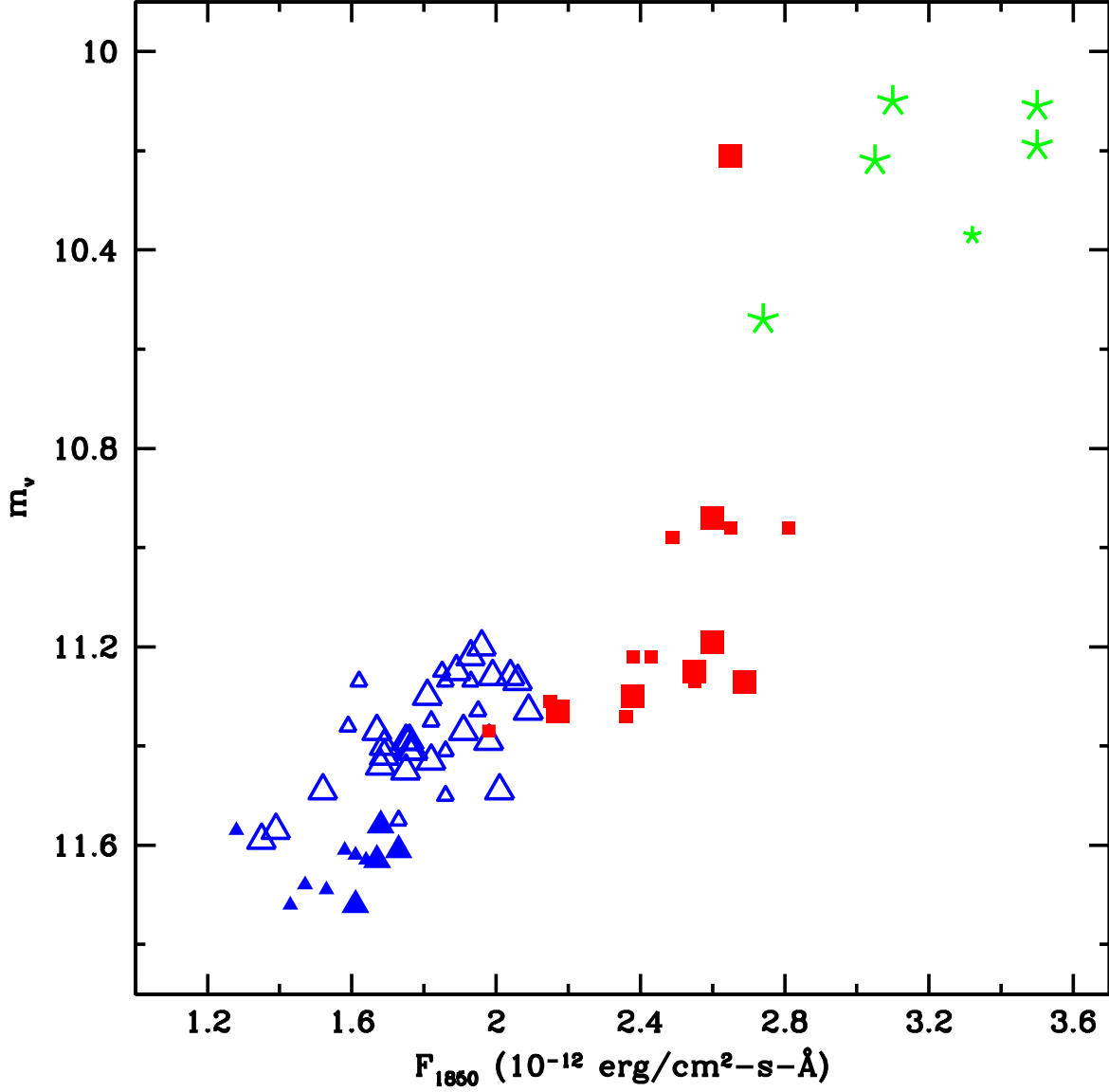


Fig. 7.— Visual magnitudes derived from the *IUE* FES counts and the continuum absolute flux values at 1850 Å. Symbols indicate: filled triangles – 1979-1981; open triangles – 1989-1991; stars – 1994; filled – 1995; Large/small symbols indicate low/high resolution spectra. The increasing trend in both wavelength regions suggests an increase in bolometric brightness.

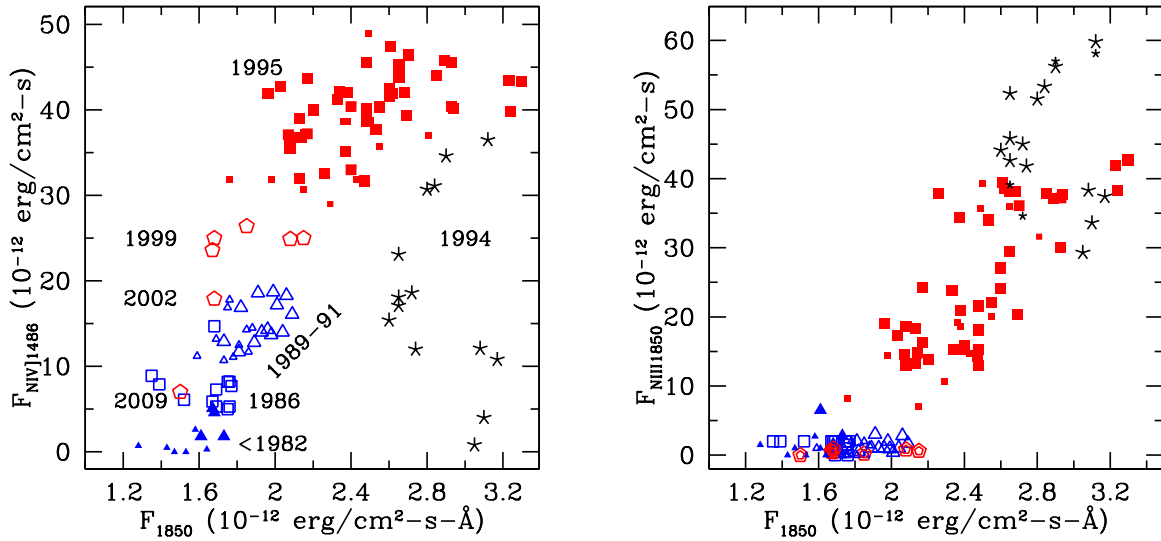


Fig. 8.— Absolute flux contained in the N IV]1486 Å (left) and N III 1750+1754 Å (right) emission lines plotted as a function of the absolute continuum flux at 1850 Å. The different epochs are indicated by different symbols: filled triangles – 1979–1981; open squares – 1986; open triangles – 1989–1991; stars – 1994; filled squares – 1995; and pentagons – 1999–2009. Large symbols correspond to values obtained from the IUE low resolution spectra and HST/STIS data; small symbols to high resolution IUE spectra. Uncertainties are $\sim 10\%$ of the flux values.

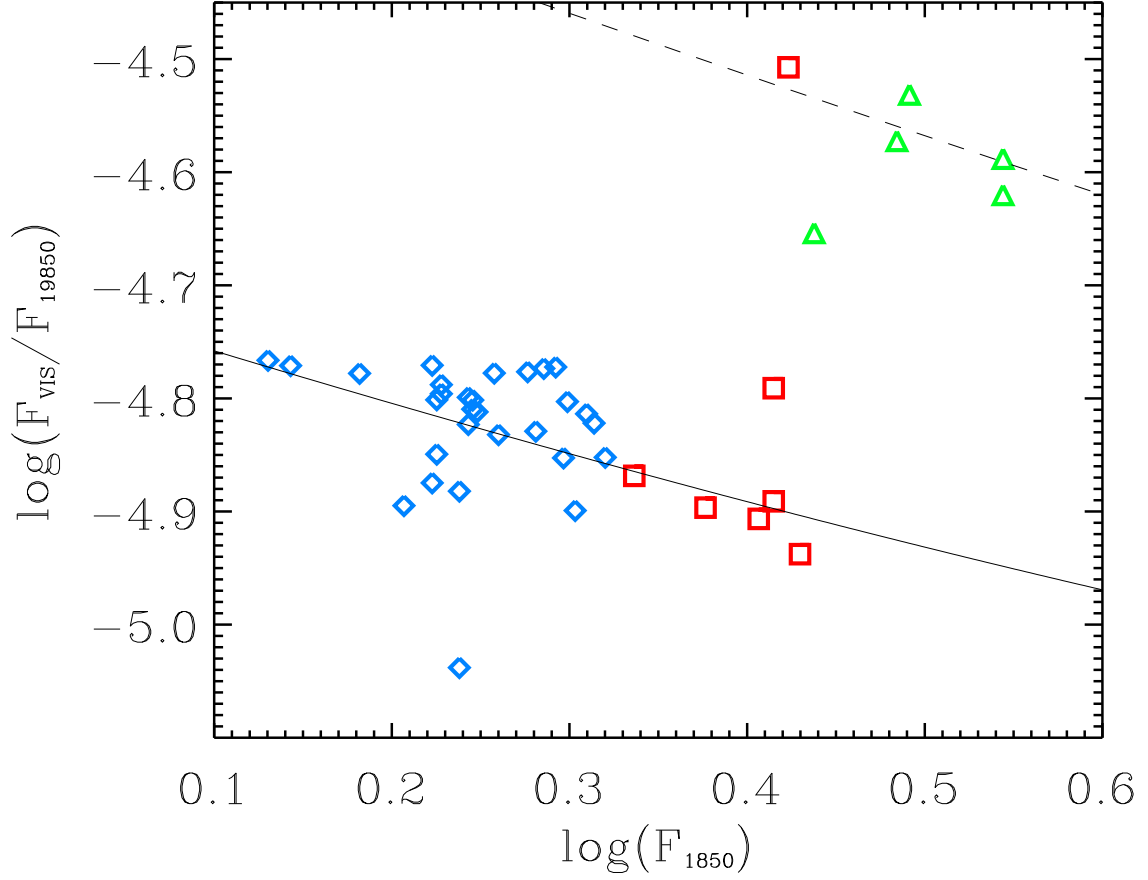


Fig. 9.— Ratio of the visual flux, F_{VIS} converted from the *IUE* FES magnitudes and F_{1850} from Table 2, plotted against F_{1850} . Small open squares - data before 1994; triangles - data of 1994; large squares - data after Jan 1995. The continuous line corresponds to the relation of F_{VIS}/F_{1850} vs F_{1850} for a black body energy distribution flux of different temperatures assuming a constant luminosity. The dashed line is the same relation but with a luminosity that is 6 times larger, implying that the 1994 eruption involved a significant change in the luminosity.

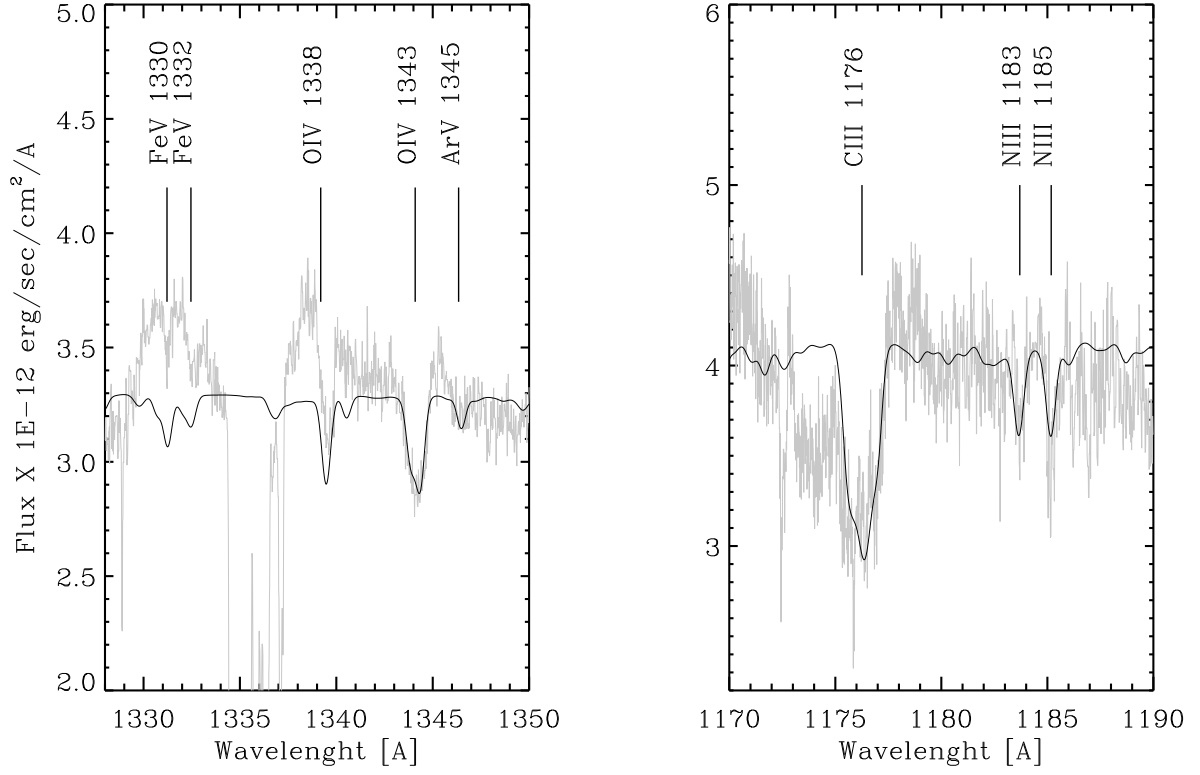


Fig. 10.— Fragments of 2002 *HST/STIS* and *FUSE* spectra (grey line) compared with the *Star C* model (black line). The model spectrum is shifted to the level of the observed spectrum which is a sum of *Star A* and *Star C* fluxes.

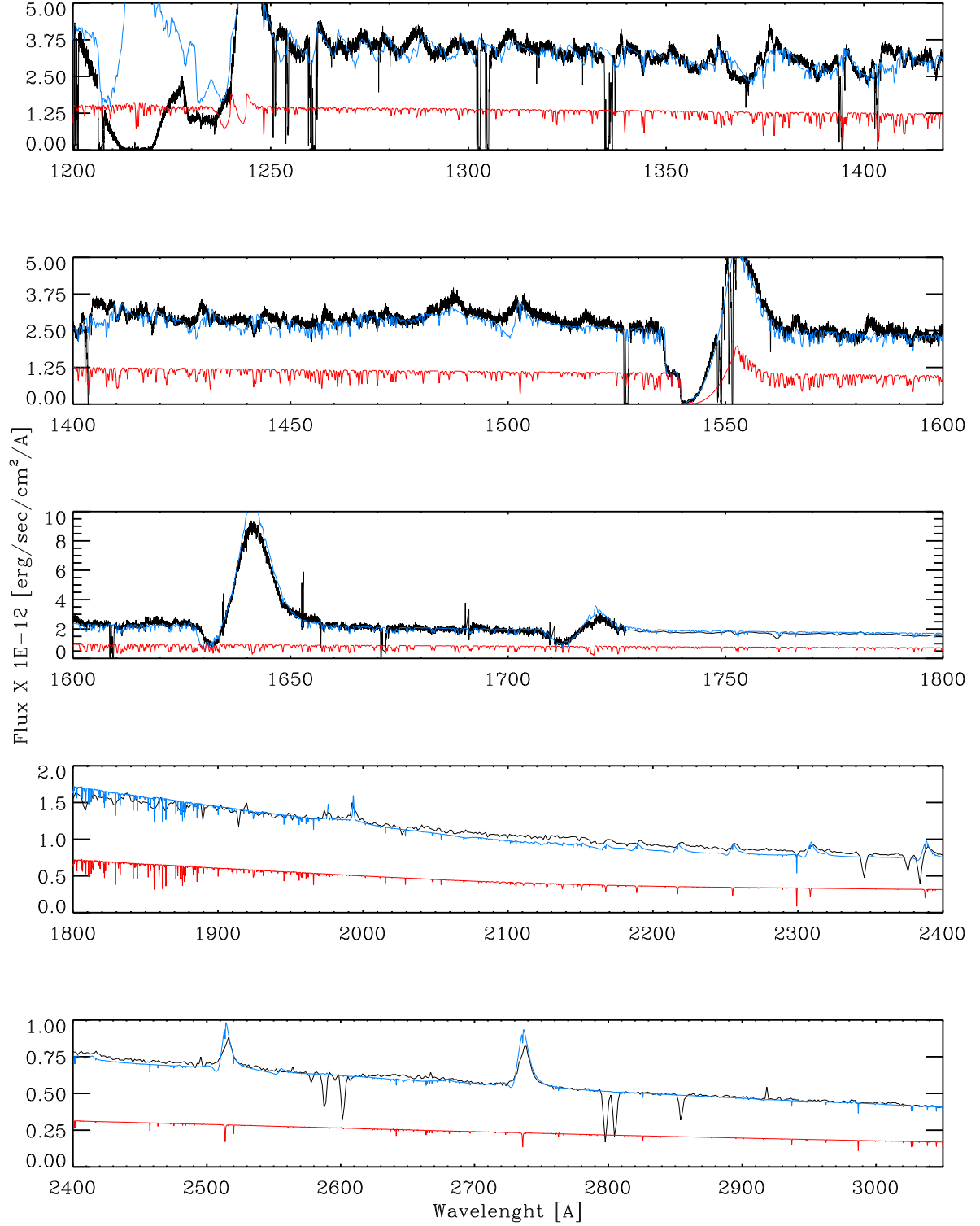


Fig. 11.— Comparison between the *HST/STIS* spectrum obtained in September 2009 (black) and the sum of the current best model for *star A* at this epoch and *star C* model. The red line represents the computed spectrum of *star C* alone. Notice the coincidence of the *star C*'s continuum and the step in the blue wind of the C IV 1548/50 Å P Cyg absorption.

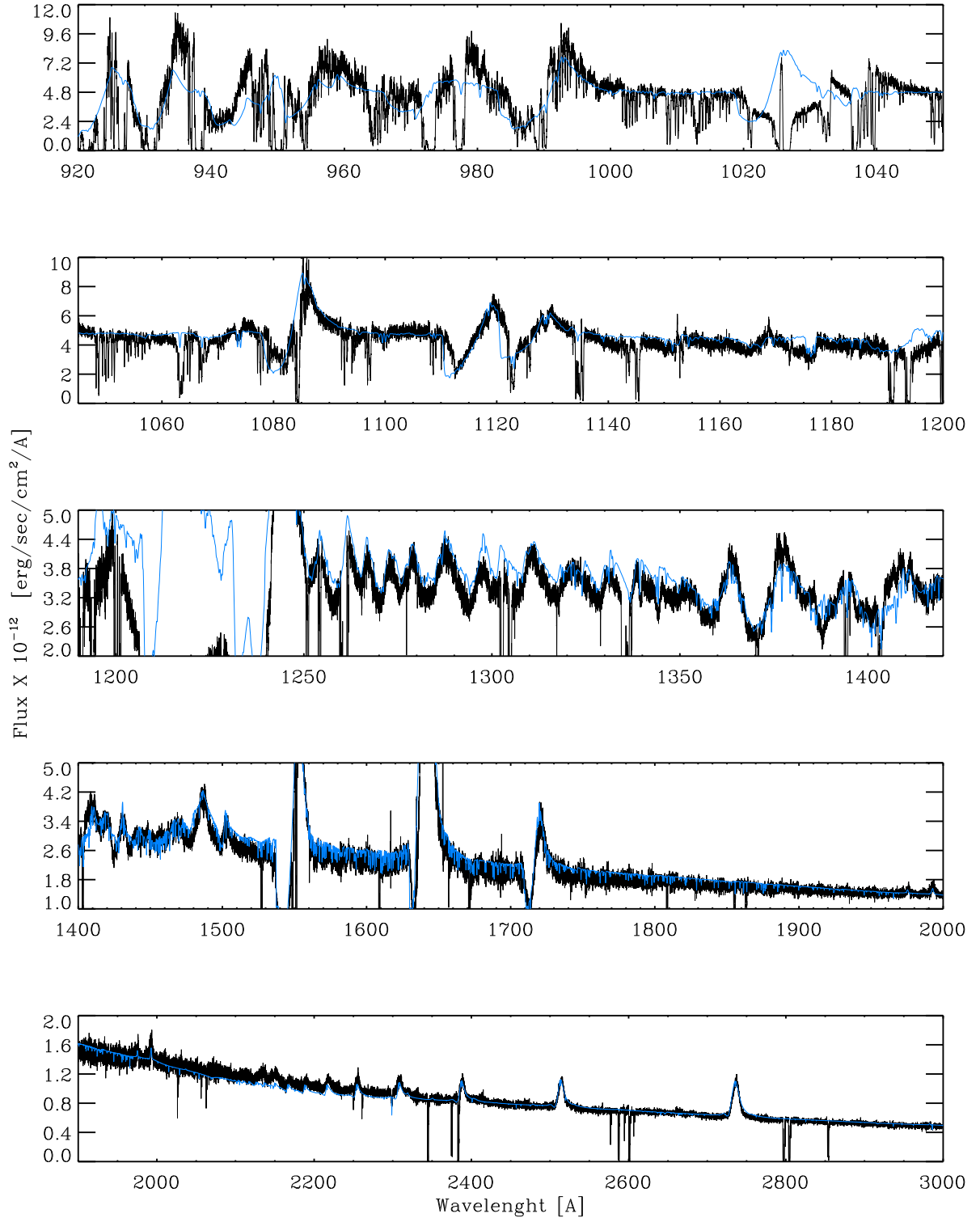


Fig. 12.— As if Fig. 13 but for the April 2002 epoch.

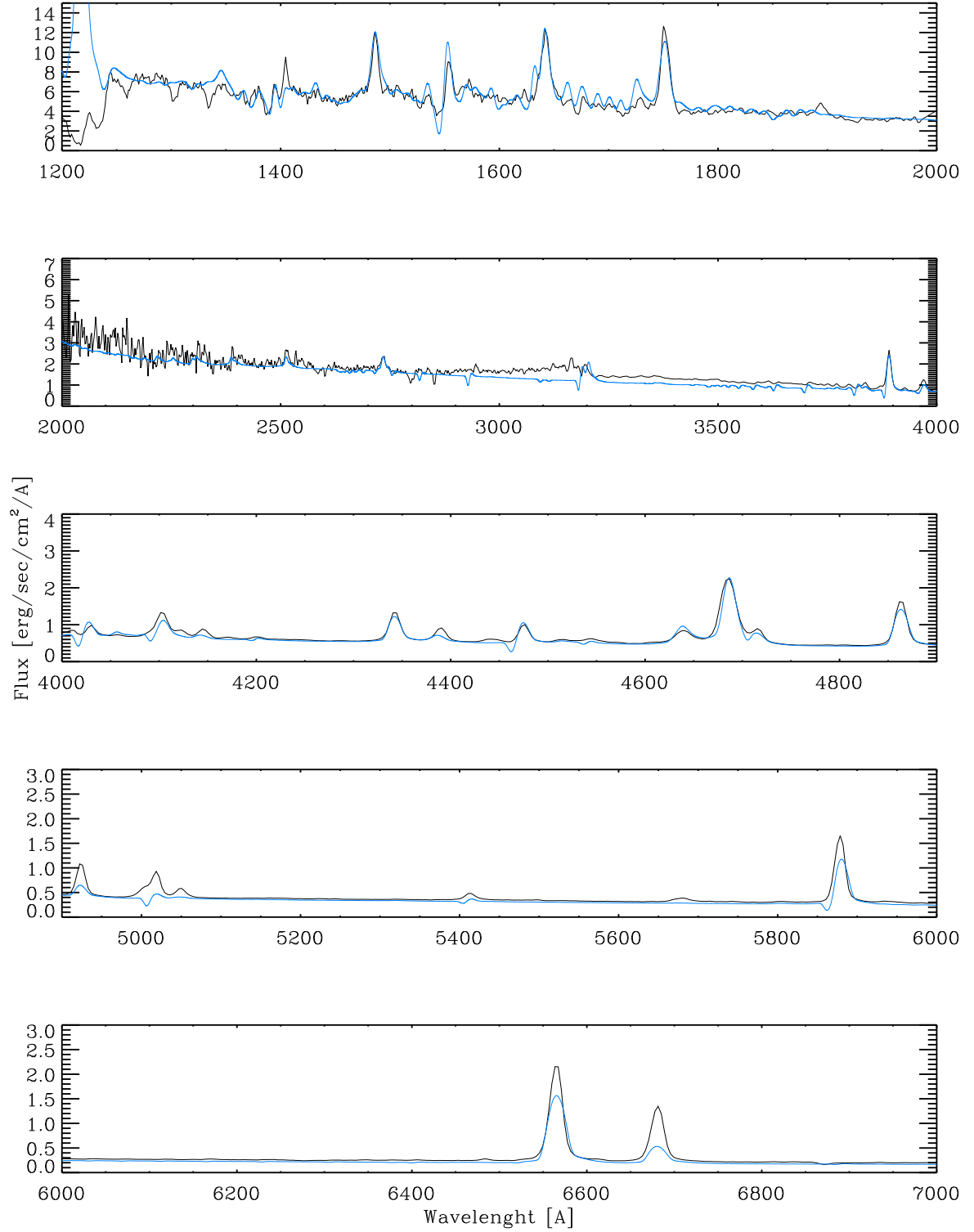


Fig. 13.— Comparison between the spectrum obtained on December 30, 1994 (black) and the sum of the current best model for *star A* at this epoch and *star C* model (blue). The singlet He I lines are underestimated while the triplet lines are well reproduced.

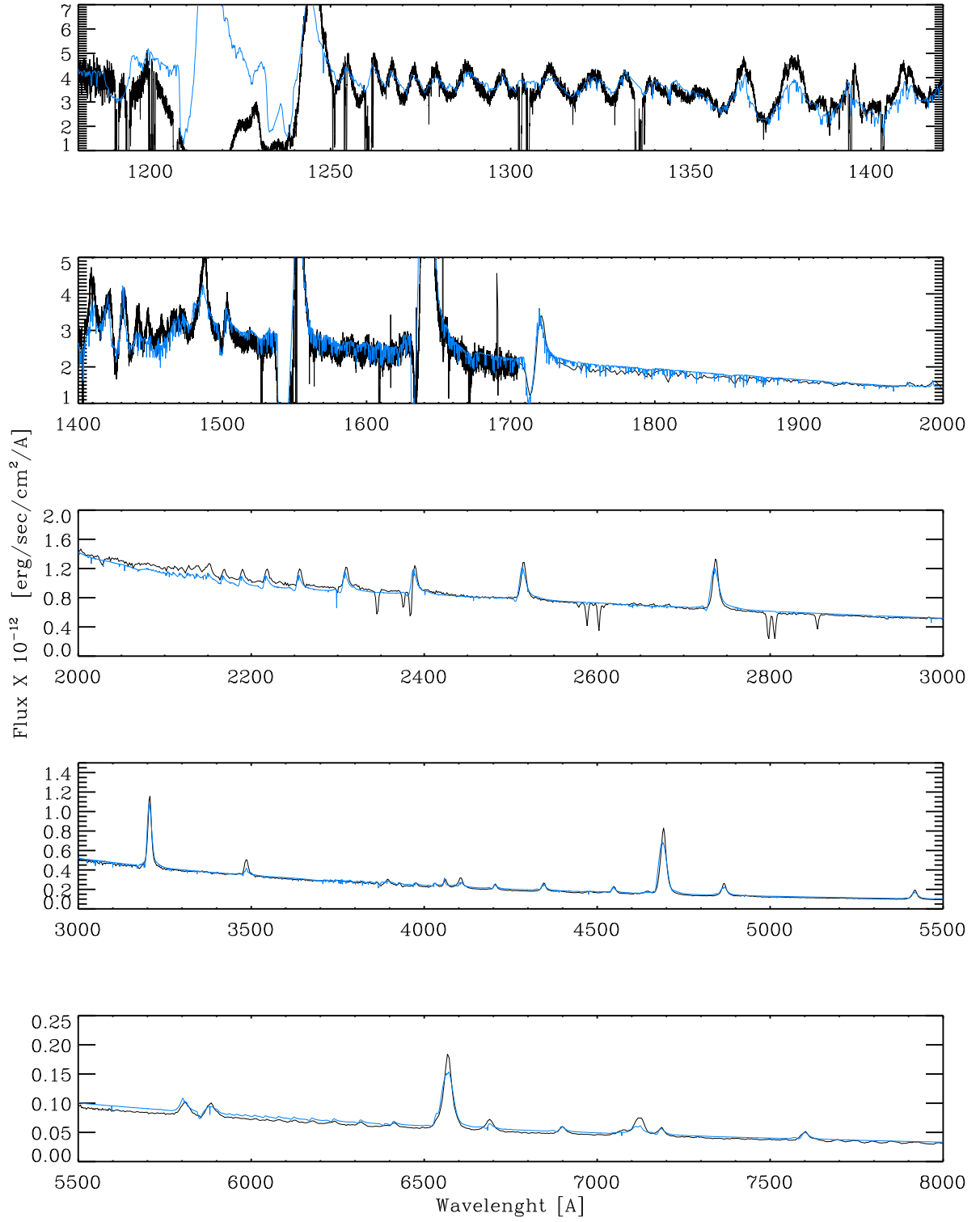


Fig. 14.— As if Fig. 13 but for the April 2000 epoch.

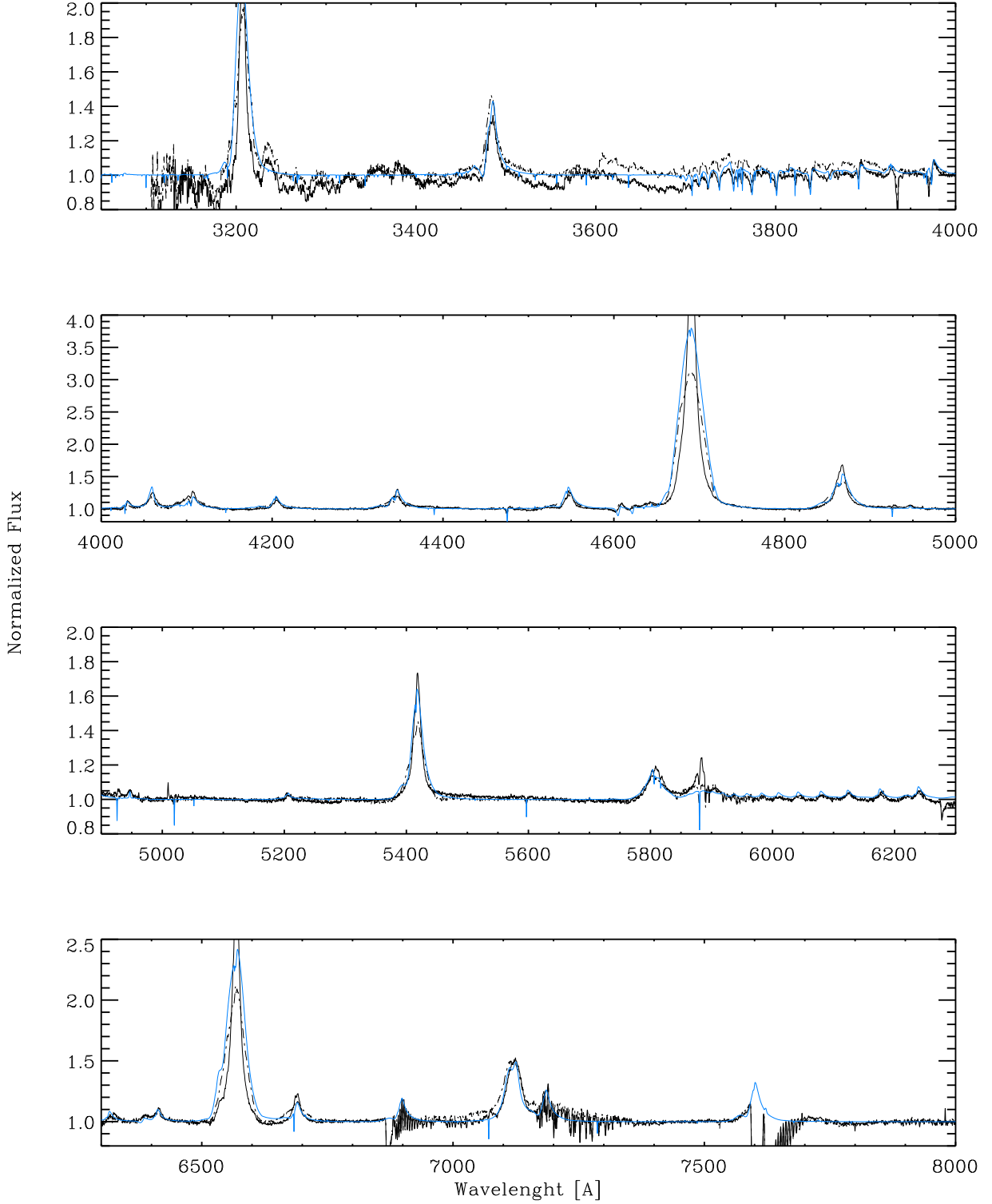


Fig. 15.— As in Fig. 11 but for the optical region. The spectrum is affected by the presence of strong telluric absorption lines in 6850Å, 7200Å and 7550Å. The observed profile of He II 4686Å and H α is much narrower than the model spectrum. Breysacher et al. (1982) showed that He II 4686 Å changes its profile with the orbital period being narrower at the eclipses. The model show that the line width outside the eclipse correspond to the UV P Cyg lines and the emission lines are much broader. The interpretation of this effect is discussed in the text.

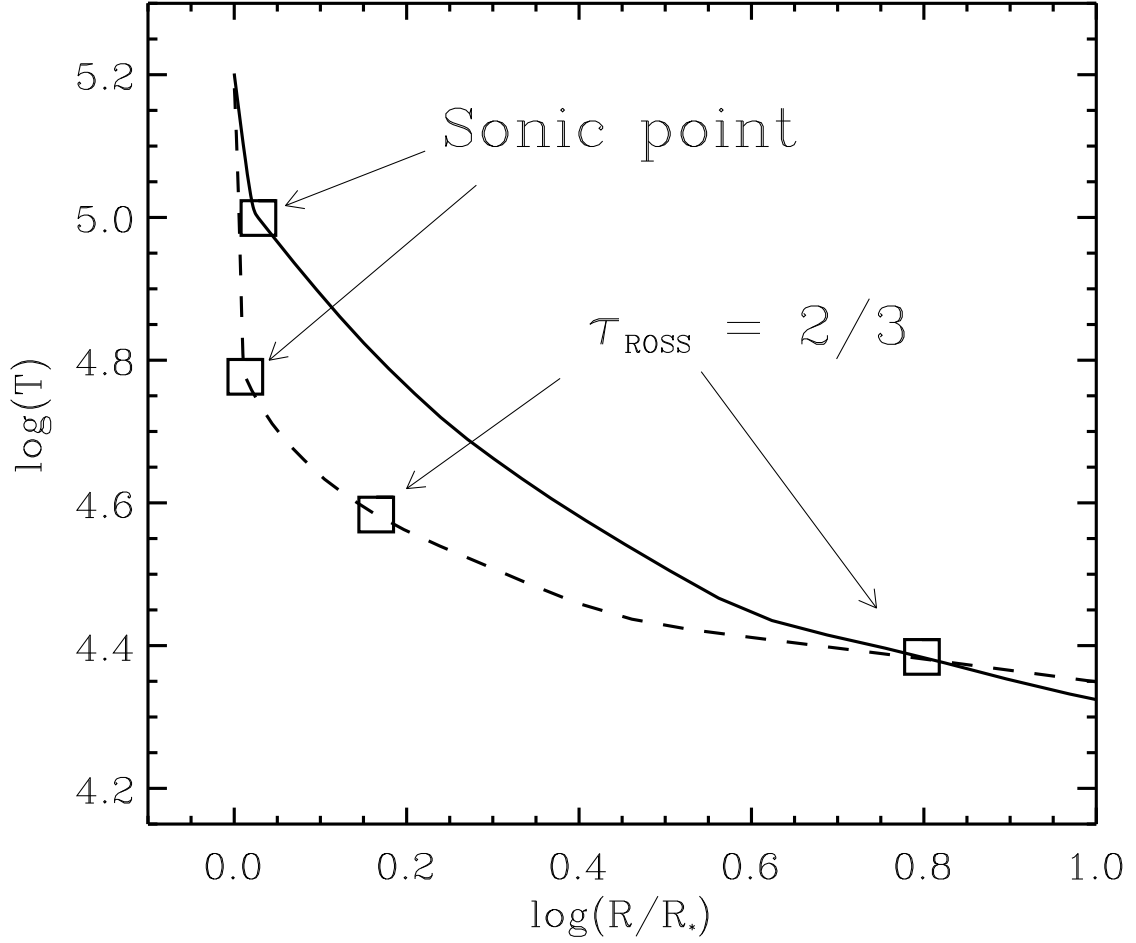


Fig. 16.— Temperature distribution in the 1994 (solid line) and 2009 (dashed line) models. The positions of the sonic point and the continuum forming regions ($\tau_{\text{Ross}} = 2/3$) are indicated. The lower mass loss rate in the 2009 model moves the continuum-forming region inward.

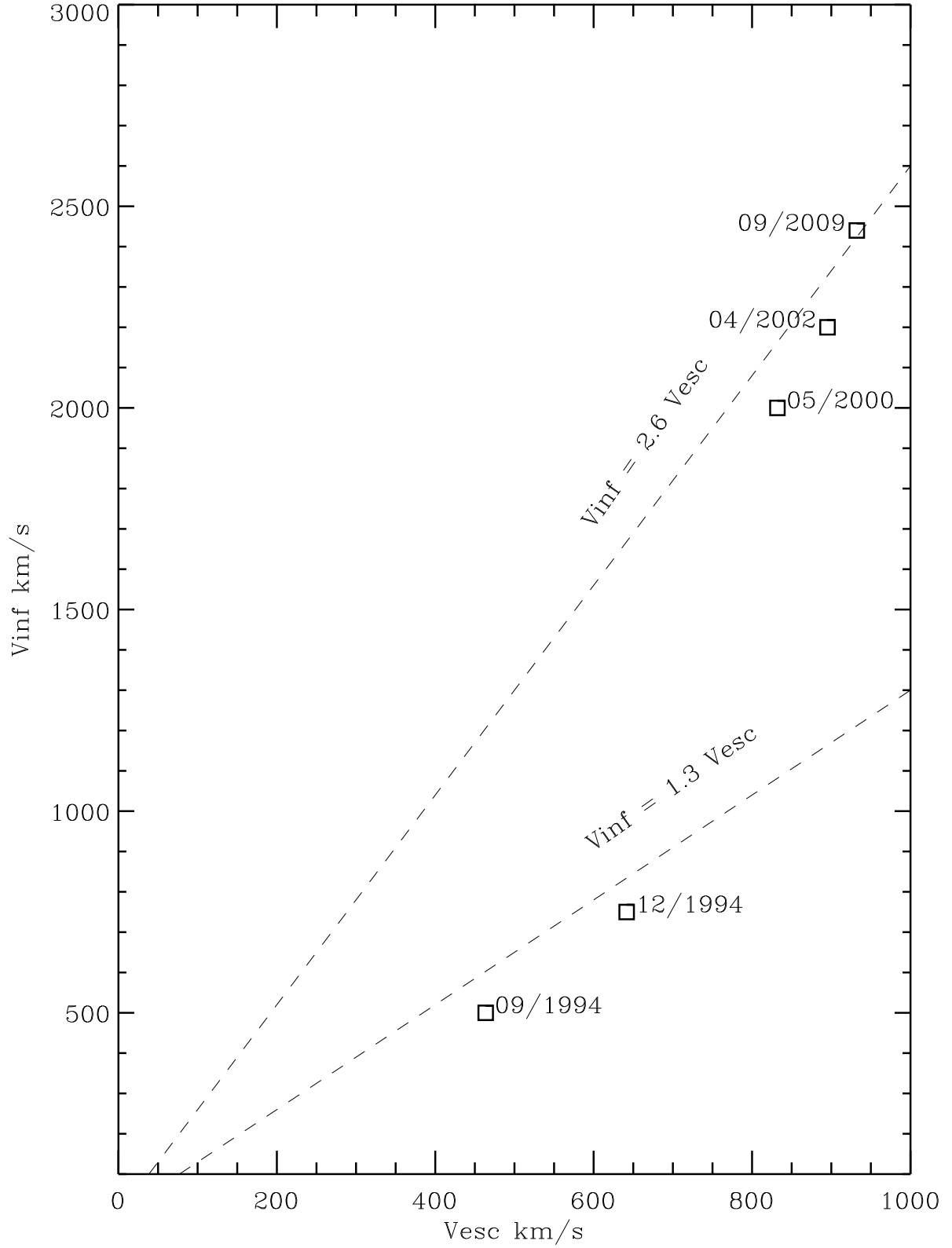


Fig. 17.— The relation between V_{∞} and V_{esc} at different epochs.